

Instituto Tecnológico de Costa Rica

Escuela de Ingeniería en Electrónica



Segmentación de imágenes de resonancia magnética para generar superficies de piel  
(Segmentation of MR images for skin surface model generation)

Informe de Proyecto de Graduación para optar por el título de Ingeniero en  
Electrónica con el grado académico de Licenciatura

Alexander Singh Alvarado

Cartago, Febrero 2006



**INSTITUTO TECNOLÓGICO DE COSTA RICA**  
**ESCUELA DE INGENIERÍA ELECTRÓNICA**  
**PROYECTO DE GRADUACIÓN**  
**TRIBUNAL EVALUADOR**

Proyecto de Graduación defendido ante el presente Tribunal Evaluador como requisito para optar por el título de Ingeniero en Electrónica con el grado académico de Licenciatura, del Instituto Tecnológico de Costa Rica.

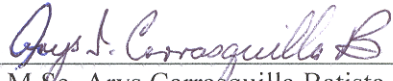
Miembros del Tribunal

Firma

  
\_\_\_\_\_  
M.Sc. Eduardo Interiano

Profesor lector

Firma

  
\_\_\_\_\_  
M.Sc. Arys Carrasquilla Batista

Profesora lectora

Firma

  
\_\_\_\_\_  
Dr.-Ing. Pablo Alvarado Moya

Profesor asesor



Los miembros de este Tribunal dan fe de que el presente trabajo de graduación ha sido aprobado y cumple con las normas establecidas por la Escuela de Ingeniería Electrónica

Cartago, Martes 31 Enero 2006



Declaro que el presente Proyecto de Graduación ha sido realizado por mi persona, utilizando y aplicando literatura referente al tema, así como la información que haya suministrado la empresa para la que se realizará el proyecto, y aplicando e introduciendo conocimientos propios.

En los casos en que he utilizado bibliografía, he procedido a indicar las fuentes mediante las respectivas citas bibliográficas.

En consecuencia, asumo la responsabilidad total por el trabajo de graduación realizado y por el contenido del correspondiente informe final.

*Alex Singh*

Alexander Singh Alvarado

Passport: 0691271

Cartago, 31 Enero 2006



# Resumen

Los métodos actuales en cirugía guiada por imágenes incluyen el aro estereotáxico y sistemas ópticos que han sido diseñados para mapear la información obtenida de las imágenes y planeamientos quirúrgicos hacia la anatomía del paciente.

Actualmente en el laboratorio de radio cirugía/biología del Instituto McKnight Brain se está trabajando en el diseño de un nuevo sistema de cirugía estereotáxica. Este se utilizará para crear prototipos de máscaras hechas a la medida del paciente.

Para el desarrollo de estas máscaras se requiere una representación confiable de la superficie de la piel. El molde o máscara será diseñado basándose en ésta superficie generada a partir de la segmentación de imágenes obtenidas por MRI (imágenes de resonancia magnética).

Este tipo de imágenes presentan varios problemas. Estos incluyen inhomogeneidades en la intensidad a través de los cortes axiales y una relación señal a ruido baja. Debido a estos problemas la detección de los bordes basado solamente en el nivel de grises lleva a resultados incorrectos en la identificación de la superficie de la piel y por ende en el diseño de la máscara.

El propósito de este proyecto es la implementación de un algoritmo de segmentación para un conjunto completo de imágenes MRI que identifique el borde de la piel con una precisión de  $\pm 2\text{mm}$  y en menos de 5 minutos. Bajo éstas condiciones una máscara de dimensiones confiables puede ser diseñada.

En el campo de imágenes médicas varias técnicas de segmentación pueden ser aplicadas incluyendo: region growing, watersheds, level set y active contours. Debido a las características de las MRI los ASM (active shape models) han sido elegidos.

Los ASM se basan en un conjunto de imágenes de entrenamiento. De éstas imágenes se captura la variabilidad en las formas. El modelo generado junto con el método de deformación constituyen un algoritmo robusto y eficiente para la detección de contornos.

Palabras claves:

modelo de forma, resonancia magnética, detección de piel, Segmentación.



# ABSTRACT

Current methods in image guided surgery include the stereotactic head ring and optical systems which have been designed to map the information obtained from images and surgery planning on to the patients anatomy.

The radio surgery/biology laboratory at the McKnight Brain Institute is currently working on a system to design and create rapid prototyping models for image guided surgery which have economical and functional advantages over currently used methods.

In order to create these models a 3D representation of the human skin surface is necessary. The fixture or model will be designed based on this surface, which can be derived from segmenting an MRI (Magnetic Resonance Image) data set.

MR images present various problems, including intensity inhomogeneities along the slices and a low signal to noise ratio. These are a consequence of technical aspects in the image reconstruction. Because of these problems segmentation based on thresholding does not lead to a correct identification of the skin border.

The purpose of this project which extends from the rapid prototyping system is toward the design and implementation of a segmentation algorithm that will identify the skin border with a precision of  $\pm 2\text{mm}$  and in less than 5 minutes for every data set. Under these conditions a reliable fixture can be designed in the aid of stereotactic surgery.

In medical imaging various segmentation techniques are employed, including region growing, watersheds, level set and active contours. Because of the MR image characteristics the active shape model approach has been selected. Combining shape restrictions and image-based information for border detection.

Key words:

Active shape models, magnetic resonance image, head contour, segmentation.



# Acknowledgments

I would like to thank Dr. Frank Bova for his trust and for the opportunity to work at the radio surgery/Biology laboratory.

To my new friends Dr. Didier Rajon, Bárbara Garita and Atchar Sudhyadhom for their advice and help during the preparation of this thesis. I would specially like to thank my adviser Dr.-Ing. José Pablo Alvarado Moya, who inspired my curiosity into image processing and helped me with my first steps.

Finally I'd like to thank my dear friends Suresh, Eric, Samir and Carlos, and my family for their support during the project.

Alexander Singh Alvarado

Gainesville, 01.31.2006



# Contents

<b>1</b>	<b>INTRODUCTION</b>	<b>1</b>
1.1	Problem statement . . . . .	1
1.1.1	Problem Context . . . . .	1
1.1.2	Problem Definition . . . . .	3
1.2	Solution Proposed . . . . .	4
1.3	Structure of this work . . . . .	5
<b>2</b>	<b>GOAL &amp; OBJECTIVES</b>	<b>7</b>
2.1	Goal . . . . .	7
2.2	General Objective . . . . .	7
2.3	Specific Objectives . . . . .	7
<b>3</b>	<b>THEORETICAL FRAMEWORK</b>	<b>9</b>
3.1	Research area description . . . . .	9
3.1.1	NMR (Nuclear Magnetic Resonance) . . . . .	9
3.1.2	MRI (Magnetic Resonance Image) . . . . .	18
3.2	Current project state . . . . .	21
3.2.1	Fixtures . . . . .	22
3.3	Image domain segmentation techniques used in medical MRIs. . . . .	24
3.3.1	Region growing . . . . .	25
3.3.2	Watershed . . . . .	25

3.3.3	Active contours . . . . .	25
3.3.4	Active Shape Models . . . . .	26
3.4	Electronic and physical principles related to the solution . . . . .	26
<b>4</b>	<b>RESEARCH METHODOLOGY</b>	<b>27</b>
4.1	Problem recognition and definition . . . . .	27
4.2	Information gathering and analysis . . . . .	27
4.3	Evaluation of the solution . . . . .	27
4.4	Implementation of the solution . . . . .	28
4.5	Evaluation and re-design . . . . .	29
<b>5</b>	<b>SOLUTION</b>	<b>31</b>
5.1	Solution selection . . . . .	31
5.2	Active shape models . . . . .	38
5.2.1	Principal Component Analysis (PCA) . . . . .	38
5.2.2	Shape modelling . . . . .	41
5.2.3	Landmarks . . . . .	43
5.2.4	Training set . . . . .	43
5.2.5	Model morphing . . . . .	45
5.2.6	Initialization . . . . .	48
5.2.7	Multi-resolution framework . . . . .	48
5.2.8	ASM features . . . . .	48
5.3	3D dataset pre-processing . . . . .	50
5.3.1	Data set re-orientation . . . . .	51
5.4	3D Dataset reconstruction . . . . .	56
<b>6</b>	<b>RESULTS AND DISCUSSION</b>	<b>57</b>
6.1	ASM overview . . . . .	57
6.2	Results at specific depths in the brain . . . . .	59

6.2.1	Over the AC-PC plane: Top of the head . . . . .	59
6.2.2	Under the AC-PC plane: nose curvature . . . . .	60
6.3	Comparison obtained using thresholding and ASM . . . . .	60
6.3.1	Over the AC-PC plane: Top of the head . . . . .	61
6.3.2	Near AC-PC plane . . . . .	62
6.3.3	Under the AC-PC plane: nose curvature . . . . .	62
6.4	3D model generation . . . . .	64
6.5	Processing Time . . . . .	66
6.6	Future work . . . . .	66
6.6.1	False edge detection . . . . .	66
6.6.2	Pre-processing . . . . .	67
6.6.3	Shape variation in young patients . . . . .	67
6.6.4	Automatic landmark placement . . . . .	68
<b>7</b>	<b>CONCLUSIONS AND RECOMMENDATIONS</b>	<b>69</b>
7.1	Conclusions . . . . .	69
7.2	Recommendations . . . . .	70
<b>A</b>	<b>Glossary</b>	<b>73</b>
<b>B</b>	<b>McKNight Brain Institute description</b>	<b>75</b>
<b>C</b>	<b>Radiology and Radio Biology laboratory description</b>	<b>77</b>



# List of Figures

1.1	Magnetic Resonance Image (left). Close up at pixel level (right)	4
1.2	MR images taken at different depths in the human head.	4
1.3	Block diagram for the general solution.	5
3.1	Magnetic field induced by the spin in the proton [2].	10
3.2	Magnetic field effect over proton alignment [2].	11
3.3	Precession effect over the proton in the presence of a magnetic field [2].	12
3.4	The magnetization vector and its components.	12
3.5	T2, free induction decay time.	13
3.6	T1, return to equilibrium time.	14
3.7	Generation of the gradient field.	16
3.8	Gradient field applied to the patients body.	17
3.9	The inclination of the gradient affects the slice thickness.	17
3.10	Example of an MRI machine designed specially for patients that suffer from claustrophobia [17]	18
3.11	Example of a MRI image taken from a set with a resolution of 512 x 512 x 119.	19
3.12	The different views of the human anatomy used to analyze CT and MRIs.[14]	20
3.13	Examples of a CT (left) and MRI (right) scans.	21
3.14	Patient with a head ring [13]	21
3.15	Current graphical user interface.	22

3.16	Fixture created based on a head model. . . . .	22
3.17	Fixture created using 3D printer with the guide to hold the probe. . .	23
3.18	Example of the fixture use. . . . .	23
3.19	Zprinter 310 three dimensional printer used to create the fixtures. . . .	24
3.20	Zprinter 310 printing process. . . . .	24
3.21	Watershed algorithms based on immersion (left) and rain-fall (right). .	25
3.22	Example of how the snake adapts to the specific regions. . . . .	26
4.1	Scheme for the evaluation of the segmentation algorithms . . . . .	28
5.1	Marr-Palmer’s computational vision framework for human perception.	31
5.2	Example of an MRI scan. . . . .	33
5.3	Examples of two MR images taken from different scanners. . . . .	33
5.4	Partial volume effect. . . . .	34
5.5	The inverse Fourier transform will cause bottom slices to reappear on the top slices. . . . .	35
5.6	Block diagram for the general solution. . . . .	37
5.7	Illustration of the eigenvectors for a set of 3D points. . . . .	39
5.8	Effect of varying the elements in the B vector. The shapes have been scaled and translated in order to be displayed. . . . .	42
5.9	Landmark assignment near the tip of the nose. . . . .	43
5.10	Distribution of the patients by age at treatment in the radiosurgery database at the McKnight Brain Institute. . . . .	44
5.11	Point based displacements. . . . .	45
5.12	Gray level profile creation based on adjacent points. . . . .	46
5.13	Profile scanning. . . . .	47
5.14	The suggested shape in red and the shape when the constraints are applied in blue. Figures 1a and 2a show this process at the nose level. Figures 1b and 2b are near the AC-PC plane. . . . .	47
5.15	Multi-resolution framework. . . . .	49

5.16	Intermediate tests applied to the ASM during the implementation. The test image was transformed by adding noise, warping and smoothing.	49
5.17	Setup in the MR scanning room.[8]	50
5.18	The patients head can be tilted as seen in the sagittal view (lower left).	51
5.19	3-D dataset interpreted in a world coordinate system.	52
5.20	Location of the anatomical landmarks. [6]	52
5.21	Identification of the landmarks.	53
5.22	Coordinate system defined by the anatomical landmarks.	54
5.23	Coordinate transformation.	55
5.24	Basics of trilinear-Interpolation.	56
6.1	Active shape model initialization.	57
6.2	Active shape model converging at a resolution of 128x128.	58
6.3	Active shape model converging at a resolution of 256x256.	59
6.4	Active shape model converging at a resolution of 512x512.	59
6.5	ASM converging on a slice near the top of the head.	60
6.6	ASM converging on a slice under the AC-PC plane.	60
6.7	Superposition of the mask generated by the ASM and thresholding over the CT reference for a slice near the top of the head. Blue: CT reference. Red: mask generated by thresholding. Green: mask generated by the ASM.	61
6.8	Superposition of the mask generated by the ASM and thresholding over the CT reference for a slice above the AC-PC plane. Blue: CT reference. Red: mask generated by thresholding. Green: mask generated by the ASM.	62
6.9	Superposition of the mask generated by the ASM and thresholding over the CT reference for a slice at the nose level. Blue: CT reference. Red: mask generated by thresholding. Green: mask generated by the ASM.	62
6.10	Procedure to determine how well the segmentation algorithms perform.	64
6.11	Qualitative comparison between the ASM results (left) and thresholding (right).	65

6.12 Surface generated by the ASM. . . . .	65
6.13 Qualitative comparison between the ASM results and thresholding applying superposition. . . . .	66
6.14 ASM converging on a false edge. . . . .	67

# List of Tables

3.1	Magnetic resonance properties of medically useful nuclei [2]. . . . .	10
3.2	Gyromagnetic ratio for useful elements in magnetic resonance [2]. . . .	12
3.3	T1 and T2 relaxation constants for several tissues [2] . . . . .	15
6.1	Sum of the square of the border differences between the segmentation results and the reference CT scan (15 points were used). . . . .	63



# Chapter 1

## INTRODUCTION

### 1.1 Problem statement

#### 1.1.1 Problem Context

The radio surgery and radio biology laboratory at the McKnight brain institute is currently developing a system to design and create rapid prototyping models for image guided surgery. The following description is based on the grant proposal NIH-NIBIB Grant # 5R01EB2573-3 [13].

The next generation of surgical planning applies the optimized virtual plans at the time of surgery. This is possible by evaluating alternate surgical approaches through the manipulation of the patients specific virtual 3D data set. The ability to apply the virtual surgical plan to the real world patient at the time of surgery is termed image guided surgery.

Image guided surgery is divided in two categories, frameless and frame based.

#### **Frame based stereotactic surgery**

In frame based stereotactic or image guided surgery the reference frame will incorporate necessary trajectories for guidance including mechanical referencing to the patient at the time of surgery, guidance for initial skin incision, position and design of the required craniotomy, trajectory alignment to the large tissues and a mechanical platform used to mount other surgical tools such as retractors or skin clips.

Although very precise, the system has various disadvantages:

- Bulky obtrusive equipment.
- Technical difficulties tracking surgical instruments.
- The requirements for special scans and special training.
- Cost of replacement parts.
- Because of the pain involved in frame placement pediatric patients must undergo general anesthesia prior to frame application.

The apparatus used during diagnostic imaging contains reference fiducials that are embedded in each diagnostic image. These fiducials provide means to map the image back to the stereotactic frame's coordinate system see Figure 3.14.

### **Frameless stereotactic surgery**

Fiducial landmarks are derived from the patients own anatomical features [11]. These fiducial replace the frame based fiducials.

Rigid frame based systems such as those used in stereotactic biopsy and radiosurgery have an advantage in their rigidity and in their ability to eliminate the geometry errors.

For frame less patients the time sequence is somewhat more relaxed. When external fiducials are required, they can be applied to the patient the day prior to surgery.

When using frameless systems the shift of skin must be contemplated. For example if the medial canthus and lateral canthus are to be used as anatomic landmarks, selecting their exact position in the 3 dimensional reconstructing of the diagnostic datasheet can be influenced by:

- Type dataset CT/MR.
- Patient eyes are open continually blinking during the scan or if their eyes are closed and if so how tight.

At the radio surgery/biology laboratory an innovative model based guidance system is being developed. The aim of the rapid prototyping tool is to develop a new class of biopsy tool an operative instrument for specific individual patient needs and linked to the patients unique construct. Time from scanning to procedure is measured in hours and not days or weeks.

The proposed patient-specific, custom fabricated frame system has the potential of providing image guidance to the surgeon at the time of surgery and thereby provides a significant step toward a wider application for image guidance in neurosurgery.

This system avoids the requirements of special equipment to be present within the operating room and the guide can be applied and removed as needed.

If successful it could be applied to all cranial procedures and would result in great improvement in the accuracy of shunt placement, skin incision placement and bone flap placement making cranial neurosurgery accurate and minimally invasive. The estimated cost of materials per case is approximately \$10.

The research done in the Radio surgery and Radio Biology laboratory at the McKnight brain institute is toward the design of new fixtures for guided surgery based on MRI or CT scans that in some cases will fulfill the same task as the stereotactic frame. The overall accuracy goal for these fixtures lies within  $\pm 2\text{mm}$ .

At this moment the system under development presents an inaccurate reconstruction of the three dimensional model based on the MRI, therefore the fixtures which are designed in accordance to this model are not reliable. The segmentation algorithm being used to determine the head contour is based on a Gaussian filter and gray level threshold.

### **1.1.2 Problem Definition**

Magnetic resonance images present various problems that make segmentation a difficult task. Figure 1.1: shows a typical MR image in which the following problems can be identified:

- Low signal to noise ratio.
- Intensity inhomogeneities.
- Low contrast between the skin surface gray level and the air immediately outside the patients contour.

The image quality is a reflexion of the technical limitations in MRI scanning. These characteristics can lead to segmentation errors such as false edge detection, over tessellation and gaps in borders and edges.

In this project the segmentation process will have to deal with various images that correspond to different depths in the human head anatomy, therefore the head contour will vary in shape and size as seen in Figure 1.2.

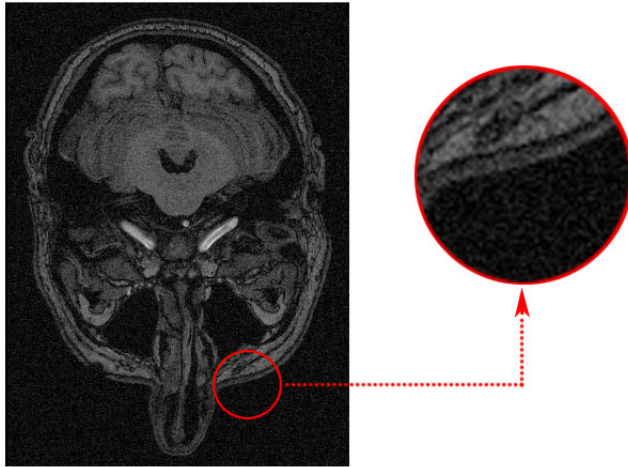


Figure 1.1: Magnetic Resonance Image (left). Close up at pixel level (right)

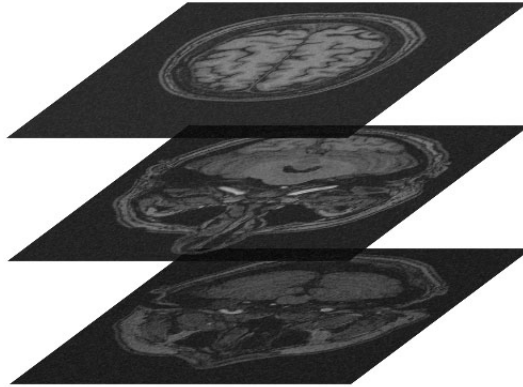


Figure 1.2: MR images taken at different depths in the human head.

If a slice is taken close to the top of the head the contour will resemble that of an oval. As the depth progresses, the eyes, ears and nose appear changing the boundary. Because of the shading effect the gray levels at the edges will also vary depending on the depth.

The problem lies in the difficulty of processing the images due to the quality of MR scans and the variation of the head contour.

## 1.2 Solution Proposed

There are hundreds of algorithms applicable to image segmentation. For edge detection these are very difficult to fully explore due to the overwhelming number of

variations of each type. The selection of an appropriate technique for a specific type of image is a difficult problem [15].

There are several factors that make it difficult to choose a segmentation algorithm, because there is no common ground from which it is possible to compare the results of each algorithm.

In order to quantify the performance of a segmentation method validation experiments are necessary [21]. However there's a difficulty in implementing other people's algorithms due to the lack of necessary details [20]. The algorithms have also been designed for an specific type of image and a specific application.

By carefully analyzing the problems present in MR imaging the algorithm that best fits this task is the active shape model. But in order to make use of this segmentation technique pre-processing modules are required such as those shown in Figure 1.3.

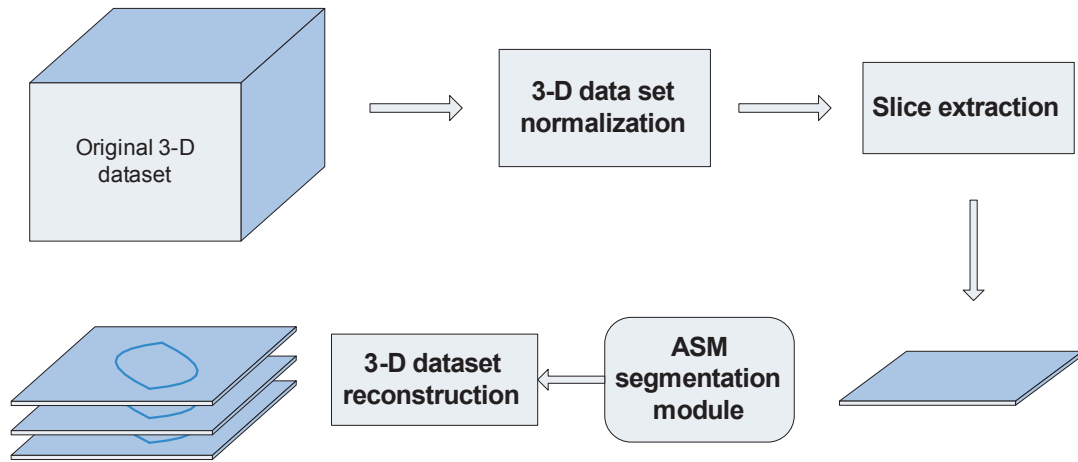


Figure 1.3: Block diagram for the general solution.

In order to validate the implementation of the algorithm empirical discrepancy [22] methods will be applied with a fused set of CT and MR images.

The CT images have a higher spatial resolution therefore the contours can be easily determined using simple segmentation algorithms. These contours can then be used as the ground truth for the evaluation function, of the segmented MR images.

## 1.3 Structure of this work

First a general description of the physics involved in nuclear magnetic resonance is explained along with the problems found in MR imaging. At the end of chapter 3 several image segmentation techniques are explained.

Chapter 4 refers to the solution itself, and justifies the selection of the ASM as the segmentation algorithm followed by a detailed description of the mathematical concepts explaining ASM.

Chapter 5 shows the results obtained from using the ASM in the segmentation of MR images and the comparison with the results obtained from the current thresholding methods.

Finally chapter 6 presents the conclusions of this work and recommendations for further projects.

# Chapter 2

## GOAL & OBJECTIVES

### 2.1 Goal

- To develop reliable fixtures and guides to be used in neurological surgery.

### 2.2 General Objective

- Develop a segmentation algorithm to identify a patients head contour in axial T1 MRIs

### 2.3 Specific Objectives

- Develop and implement a head contour detection software compatible with the rapid-prototyping system at the McKnight Brain Institute.
- Implement discrepancy evaluation methods to assess the segmentation algorithm.
- Create a detailed documentation of the developed algorithm for future revisions.



# Chapter 3

## THEORETICAL FRAMEWORK

### 3.1 Research area description

In order to understand completely the problem and the solution, certain concepts must be established.

#### 3.1.1 NMR (Nuclear Magnetic Resonance)

The following subsection on nuclear magnetic resonance is based on [2].

Magnetic resonance imaging is based on nuclear magnetic resonance (NMR). The NMR phenomenon relies on the fundamental property that protons and neutrons that make up a nucleus possess an intrinsic angular momentum called spin [12].

The proton is a charged particle with a nuclear spin that produces a magnetic dipole. An analogy can be made considering a spiral with a direct current as seen in figure 3.1. The direction of the current will define the polarity of the magnetic field.

The neutron on the other hand does not present a charge but it does have a magnetic field opposite and approximately of the same magnitude as the protons which is caused by charge inhomogeneities at sub nuclear scale.

Protons have a magnetic field that is created by this rotation. When protons and neutrons combine to form nucleus, they combine with oppositely oriented spins [12], therefore if the number of protons and neutrons in the nucleus are equal the overall magnetic field is zero. Elements constituted by an odd sum of protons and neutrons will present an net magnetic field.

Table 3.1 shows a list of biologically relevant elements that are candidates for pro-

ducing MR images [2]. From table 3.1 it can be seen that hydrogen has the highest magnetic moment and greatest abundance which makes it by far the best element for general clinical utility.

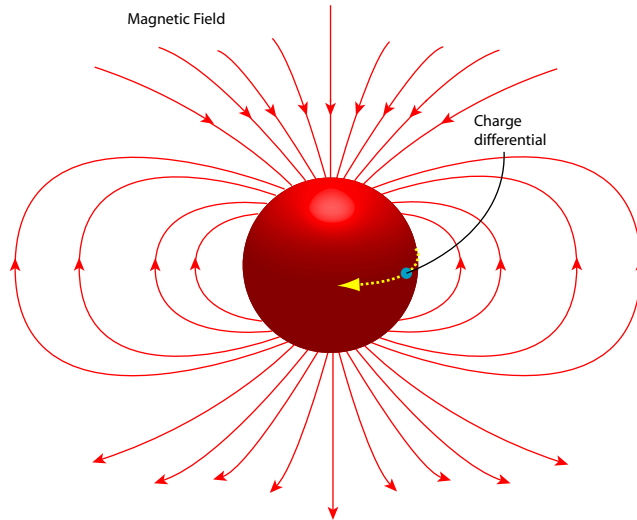


Figure 3.1: Magnetic field induced by the spin in the proton [2].

Table 3.1: Magnetic resonance properties of medically useful nuclei [2].

Nucleus	Spin Quantum Number	Isotopic Abundance	Magnetic Moment	Relative Physiologic Concentration	Relative Sensitivity
$^{12}\text{H}$	1/2	99.98	2.79	100	1
$^{16}\text{O}$	0	99.0	0	50	1
$^{17}\text{O}$	5/2	0.04	1.89	50	$9 \cdot 10^{-6}$
$^{19}\text{F}$	1/2	100	2.63	$410^{-6}$	$3 \cdot 10^{-8}$
$^{23}\text{Na}$	3/2	100	2.22	$8 \cdot 10^{-2}$	$\cdot 10^{-4}$
$^{31}\text{P}$	1/2	100	1.13	$7.5 \cdot 10^{-2}$	$6 \cdot 10^{-5}$

The human body is for the most part water and fat. Hydrogen atoms are found in abundance but because thermal energy agitates and randomizes the direction of the spin in tissue samples there is no net magnetic field. In the presence of a magnetic field the random direction of the protons will align with the external field in one of two manners, in alignment with the field (parallel) at a low-energy state or aligned against the field (anti-parallel) at a higher energy state (see Figure 3.2). Low energy

state protons are found in a ratio of 3 per million under a 1.0T field considering that a typical voxel volume in MRI contains about  $10^{21}$  protons, there are  $3 \cdot 10^{15}$  more spins in the low energy state [2].

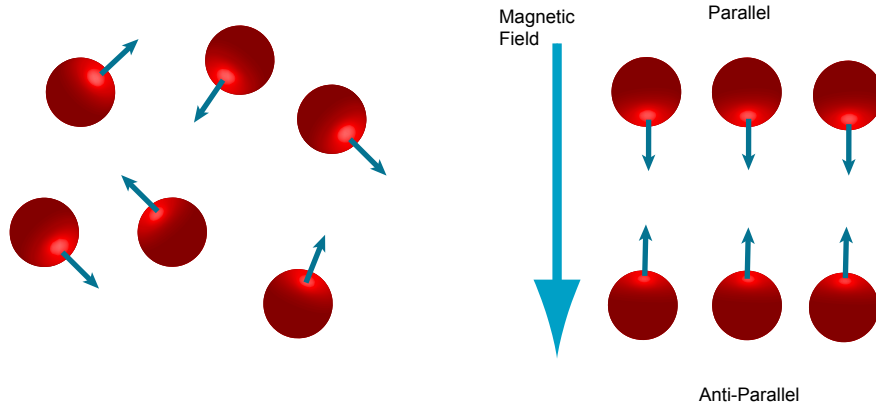


Figure 3.2: Magnetic field effect over proton alignment [2].

Another important characteristic of protons is that they also experience a torque force from the applied field that causes precession similar to how a spinning top wobbles due to the force of gravity. The angular frequency of this precession is defined by the Larmor equation (see Figure 3.3).

$$\omega = \alpha \cdot B_o \quad (3.1)$$

Where  $\alpha$  is the gyromagnetic ratio and  $B_o$  is magnetic field magnitude. Based on this equation it is seen that the resonant frequency of the protons depends on the magnetic field the proton is subject to. Each element has a unique gyromagnetic constant which allows for discrimination. Table 3.2 lists the gyromagnetic constants of elements useful in magnetic resonance [2].

The net magnetization vector  $M$  is described by three components (Figure 3.4).  $M_z$  (longitudinal magnetization) is the component parallel to the applied field. At equilibrium the longitudinal magnetization is maximum and is denoted  $M_o$ . The amplitude of  $M_z$  is determined by the excess number of protons that are in the low energy state.

$M_{xy}$  is the component perpendicular to the applied magnetic field and is also known as transverse magnetization. At equilibrium this component equals zero. When the system absorbs energy  $M_z$  is tipped into the transverse plane [2].

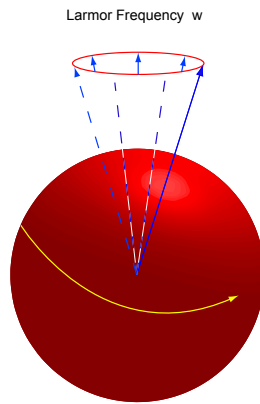


Figure 3.3: Precession effect over the proton in the presence of a magnetic field [2].

Table 3.2: Gyromagnetic ratio for useful elements in magnetic resonance [2].

Nucleus	$\alpha$ [MHz/T]
$^1\text{H}$	42.58
$^{13}\text{C}$	10.7
$^{17}\text{O}$	5.8
$^{19}\text{F}$	40.0
$^{23}\text{Na}$	11.6
$^{31}\text{P}$	17.2

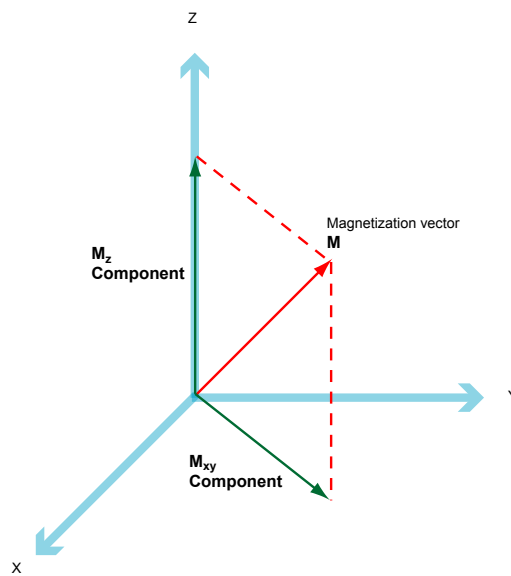


Figure 3.4: The magnetization vector and its components.

When a radiofrequency signal is synchronized to the Larmor frequency of the protons the magnetic component of the RF wave will cause the protons that are aligned antiparallel to shift into alignment with the main magnetic field by absorbing energy. Once the RF signal is removed these protons will return to their original orientation by liberating energy. The return speed depends on the type of tissue.

The amplitude and duration of the RF pulse determines the overall energy absorption, if the application of the RF signal is continued it will induce the return to equilibrium conditions.

### Free induction decay: T2

The RF pulse is applied during the necessary time for the  $M$  vector to have only one component which is transverse. Therefore once the RF signal is removed initially the  $M_{xy}$  component is maximum and a decay in the amplitude of this component begins. The decrease in the transverse vector is expressed by the equation which can also be seen in figure 3.5.

$$M_{xy}(t) = M_o e^{-t/T^2} \quad (3.2)$$

where T2 is known as the decay constant and is the elapsed time between the maximum magnitude and 37% of the peak level. The value of T2 can be used to determine the tissue type for example in non moving structures with stationary magnetic inhomogeneities have very short T2 times.

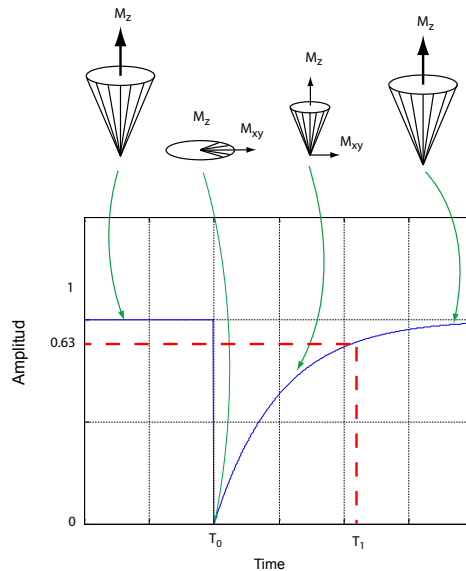


Figure 3.5: T2, free induction decay time.

## Return to equilibrium: T1

When the RF pulse is removed the  $M_z$  component starts to increase from 0 to  $M_o$  as seen in Figure 3.6. This increment is expressed by the equation:

$$M_z(t) = M_o - M_o \cdot e^{-t/T1} \quad (3.3)$$

The T1 decay time occurs relatively quickly where as the return of the excited magnetization to equilibrium takes longer. In this case T1 is the relaxation constant and is the time needed to recover the 63% of the longitudinal magnetization.

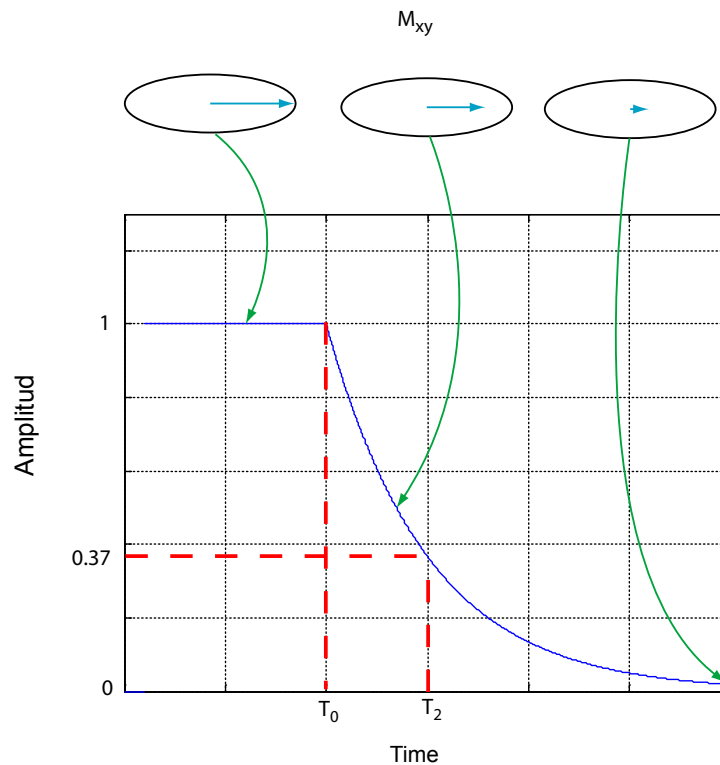


Figure 3.6: T1, return to equilibrium time.

Based on the amplitude changes that can be registered by the receiver coils T1 and T2 can be estimated in order to identify the tissue. Table 3.3 shows T1 and T2 relaxation times for several tissues.

These are estimates only, as reported values for T1 and T2 span a wide range.

Table 3.3: T1 and T2 relaxation constants for several tissues [2]

Tissue	T1 0.5T (msec)	T1 1.5T (msec)	T2 (msec)
Fat	210	260	80
Liver	350	500	40
Muscle	550	870	45
White matter	500	780	90
Gray matter	650	900	100
Cerebrospinal fluid	1800	2400	160

### Gradient Magnets

Magnetic field gradients are obtained by super imposing the magnetic fields of one or more coils with a precisely defined geometry. With the appropriate design the gradient coils create a magnetic field that linearly varies in strength versus distance over a predefined field of view as seen in figure 3.7

By generating a linear dependent field vs distance as seen in figure 3.8 the Larmor frequency will also vary linearly, this can be used for slice selection.

The slope of the gradient will also determine the slice thickness as seen in figure 3.9:

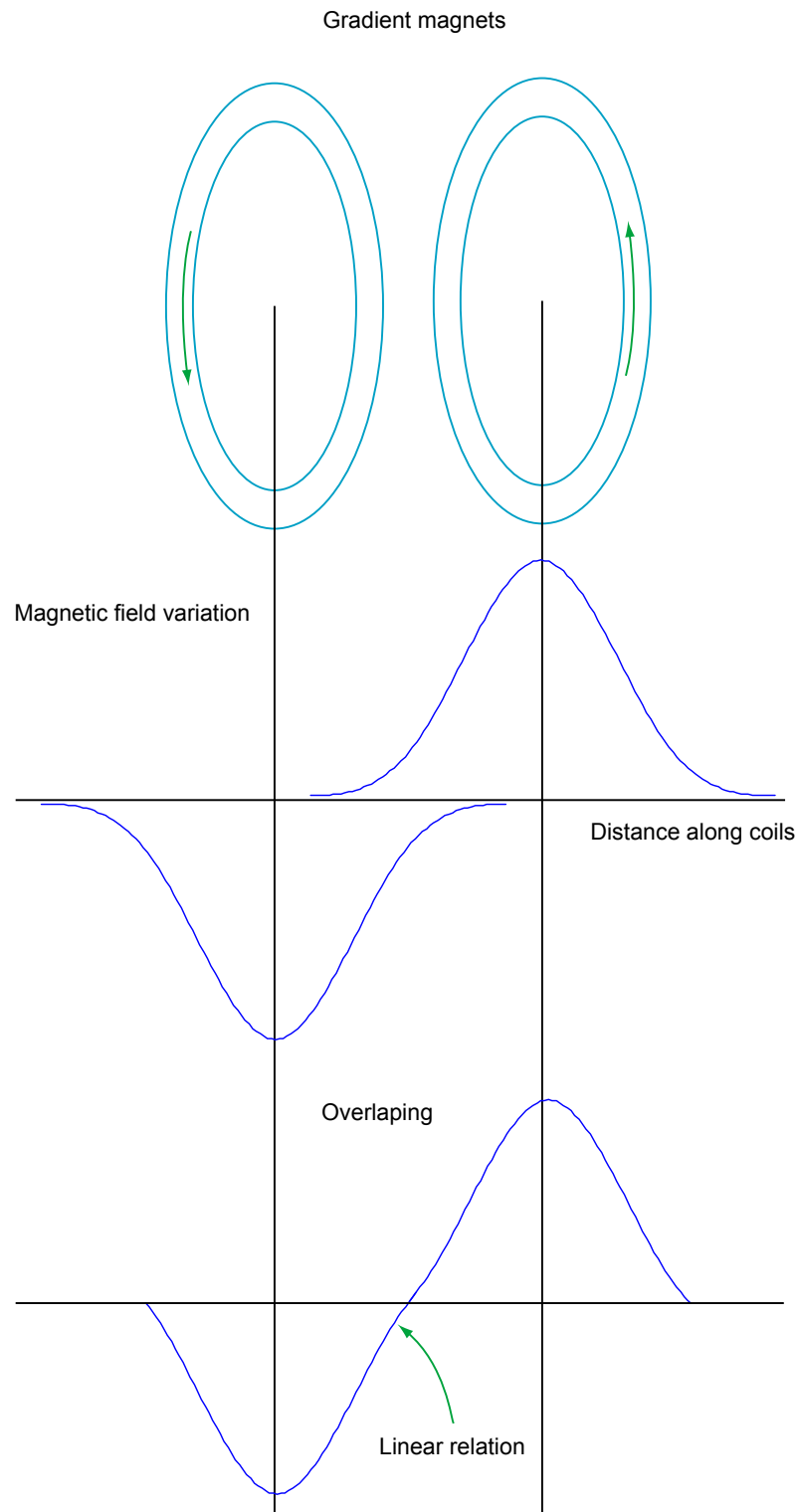


Figure 3.7: Generation of the gradient field.

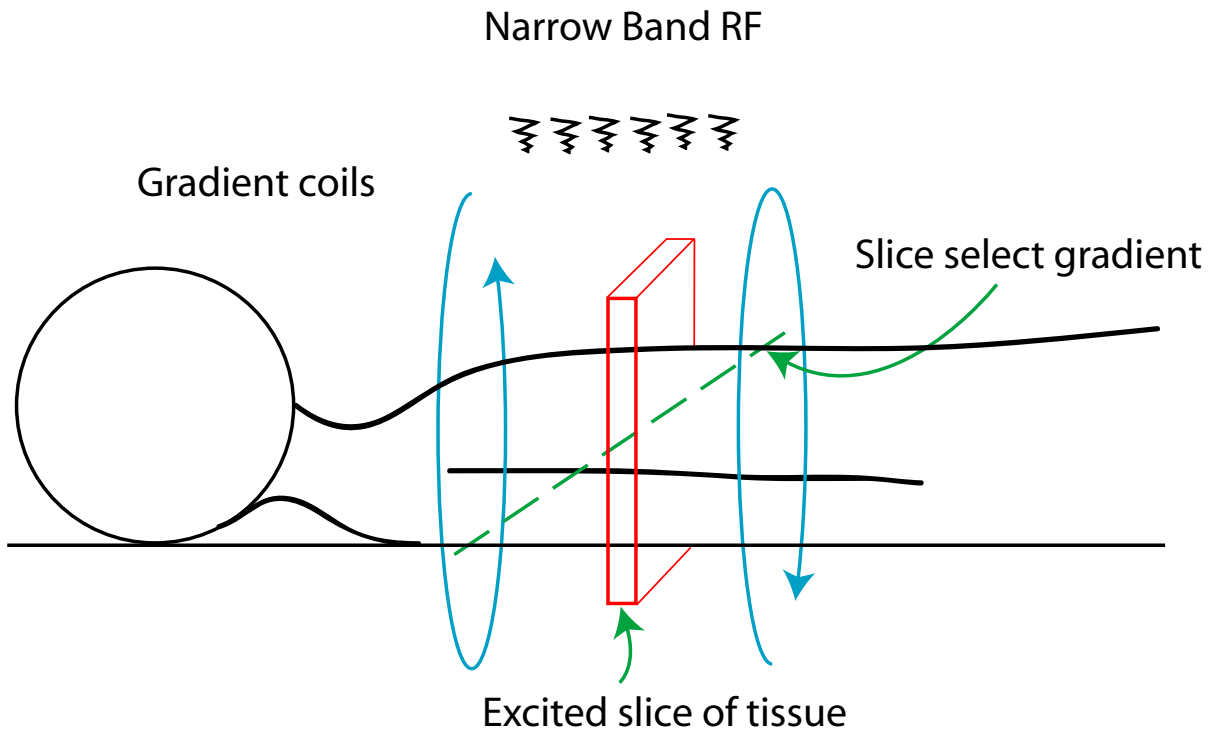


Figure 3.8: Gradient field applied to the patients body.

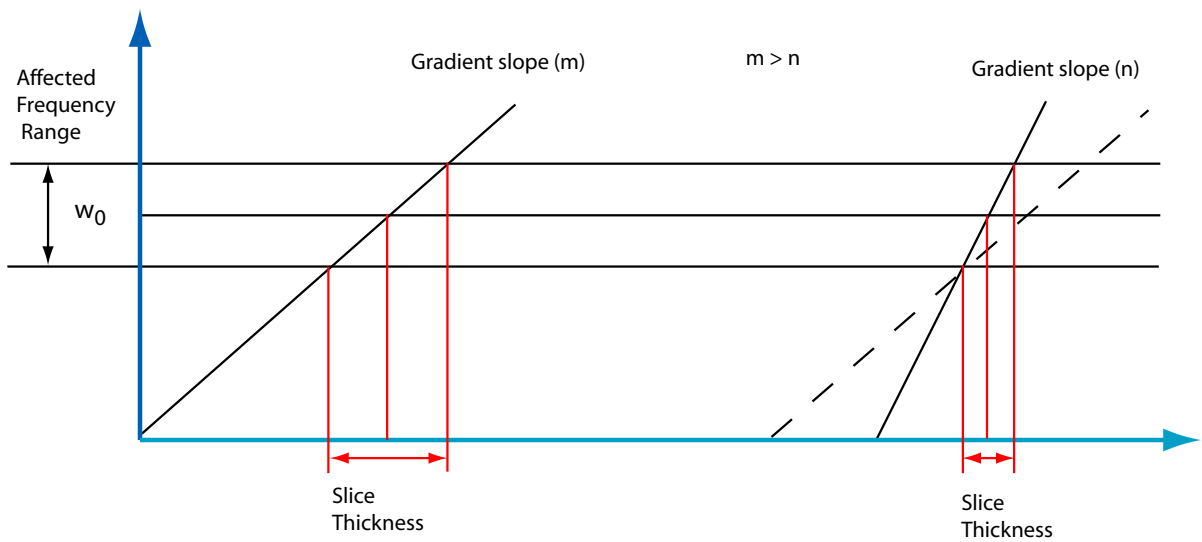


Figure 3.9: The inclination of the gradient affects the slice thickness.

### 3.1.2 MRI (Magnetic Resonance Image)

To obtain a MRI the object is placed under a constant magnetic field. The intensity of this field varies depending on the MRI equipment (ranging from  $0.1 T$  to  $4.0 T$  [2]).

Gradient magnets are used to alter the magnetic field in a specific region. This is only true for the section defined by the orientation of the gradient magnets. The position of these magnets can be used to select the orientation of the slice that will be taken from the object.

Once the area of interest has been chosen by aligning the gradient magnets, radio frequency pulses are emitted toward the region. Because the magnetic field is different in each region the Larmor frequency is also different. Therefore when the radio frequency pulses are emitted only the protons that are found inside the corresponding magnetic field will begin to resonate. When this occurs they increase their energy level by shifting toward an anti parallel position in relation to the main magnetic field. Once the radio frequency pulses are switched off the protons slowly return to their original position. While emitting energy these radio frequency signals are captured and used to determine the relaxation times, T1 and T2, which depend on the nature of the composition of the object scanned.

This technique is widely used in medical applications (Figure 3.10) because of its advantages over other imaging techniques. It is a non invasive procedure and no radiation must be submitted to the patient which is not the case for CT scans. The images obtained have a high contrast resolution, different types of tissue are easily identified which makes it a powerful instrument when identifying tumors or organ pathologies.



Figure 3.10: Example of an MRI machine designed specially for patients that suffer from claustrophobia [17]

But there are also disadvantages:

- Patients that carry any metal objects inside their bodies might not be subject to a MRI scan
- Although the contrast resolution is very high the spatial resolution is poor. In some cases a contrast substance such as gadolinium may be used to enhance visibility of certain tissue or blood vessels.

### Image Characteristics

The images obtained from a MRI scan have low quality, because of several factors [12]:

- inhomogeneity of the magnetic field.
- Radio frequency inhomogeneity can yield intensity variations in the order of 10-20%.
- Partial volume effect which occurs when multiple tissues are present in a voxel.
- Random Noise affects all MR images.

An example of a MRI image taken from a 3-D data set with a resolution of 512 pixels x 512 pixels x 119 pixels and a spacing of 0.547mm x 0.547mm x 1.5mm is seen in figure 3.11.

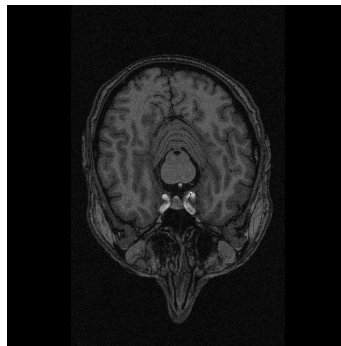


Figure 3.11: Example of a MRI image taken from a set with a resolution of 512 x 512 x 119.

Because of these technical difficulties in MR equipment, the images obtained present various problems for image segmentation:

- Borders and edges sometimes have discontinuities in their paths.
- The low signal to noise ratio makes it difficult to only use pixel based methods for segmentation.

The images that are obtained from the MRI are stored in a format called DICOM, which stands for Digital Imaging and Communications in Medicine. The purpose of this format is to provide a standard for image exchange.

Although the MRIs can be obtained in any orientation from the patient the most common slice is axial (see Figure 3.12) in accordance with CT scanners.

Images can be obtained with a different spacing in  $z$  (based on Figure 3.12) depending on the resolution that is required. This spacing usually varies from 0.5mm to 3mm, although normally 1.5mm is used. The resolution of the image given in  $x$ ,  $y$  and  $z$  coordinates is not always consistent therefore the voxels (3D pixels) do not have a symmetric distribution in the three dimensions.

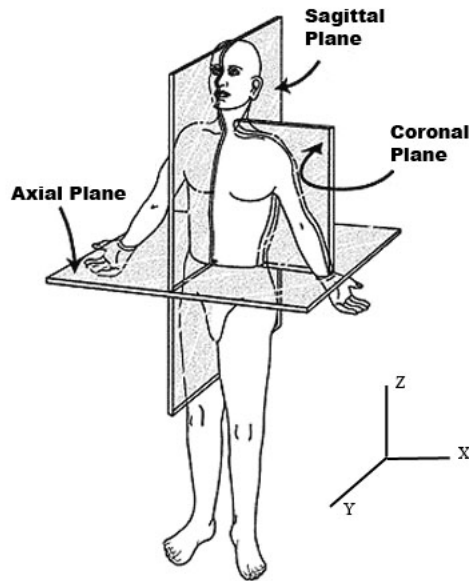


Figure 3.12: The different views of the human anatomy used to analyze CT and MRIs.[14]

Figure 3.13 shows a typical MRI taken at a specific location in the head. MRI scans are useful because tissue can be easily identified (e.g. brain tumors) as MRIs have good contrast resolution. The lack of spatial resolution makes it very difficult to identify the edges in the image. A CT scan is also done to compensate for the MRI poor resolution, but the lack of contrast resolution in the CT does not allow a clear

distinction of the tissue. Usually both scans are taken and then registered in order to identify edges and tissue.

When the patient is prepared for neurosurgery he/she must wear a head ring during the CT scan and at the moment of surgery (see Figure 3.14). Doctors can not remove the ring from the patient because its the reference between the patients anatomy and the images.

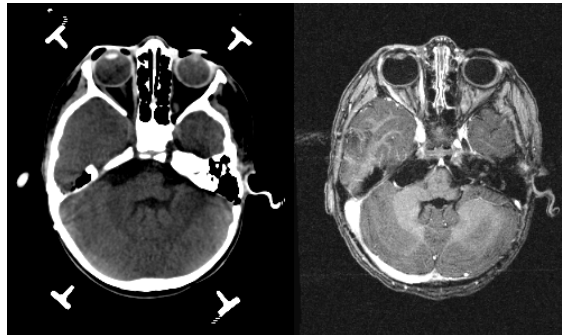


Figure 3.13: Examples of a CT (left) and MRI (right) scans.



Figure 3.14: Patient with a head ring [13]

## 3.2 Current project state

The program being used to design the fixtures has been implemented using the VTK and ITK software libraries. The graphic interface shown in Figure 3.15 allows users to navigate through the MRI images from different angles (sagittal, coronal, axial, and arbitrary). It also has the option to design the fixtures by hand-painting them directly on the 3D model seen in the lower right corner (the model is seen in Figure

3.16). Probes can be created and oriented on the images to give clinicians a better idea of the procedure at hand.

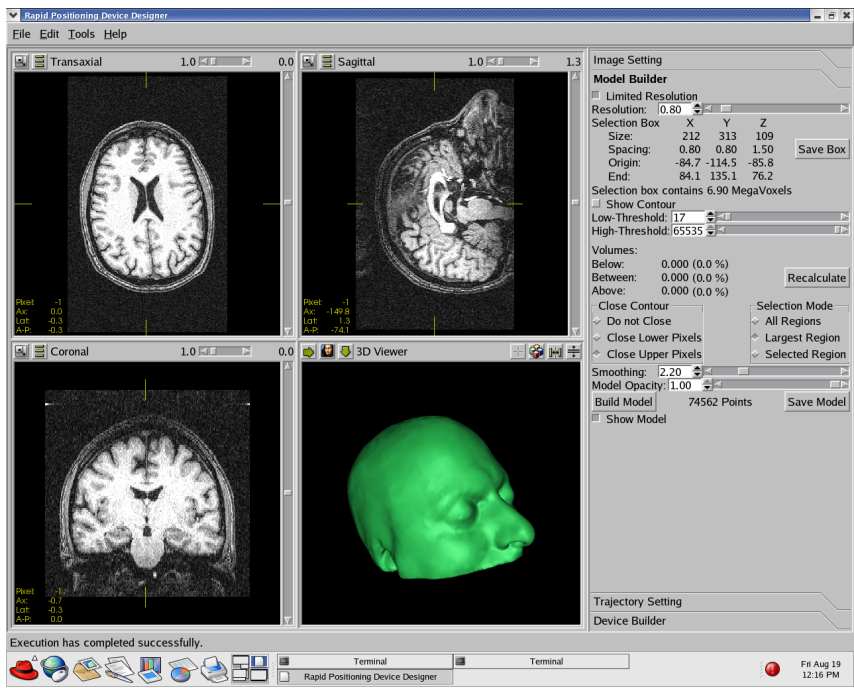


Figure 3.15: Current graphical user interface.

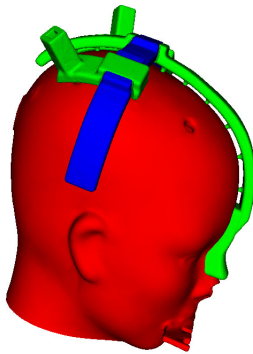


Figure 3.16: Fixture created based on a head model.

### 3.2.1 Fixtures

The fixtures refer to masks that will be placed on to the patients forehead (Figure 3.17 and Figure 3.18). These masks will have a guide that will be oriented depending on the objective of the procedure in order to lead the probe correctly.

The fixtures that will be used for testing are created using a 3d printer (see Figure 3.19). This device is composed of two bins: one holding the powder plaster and another which is empty an will eventually hold the printed 3D model. Powder is moved from one bin to another with a roller and glue is placed with a printing head on the receiving bin. This is illustrated in Figure 3.20

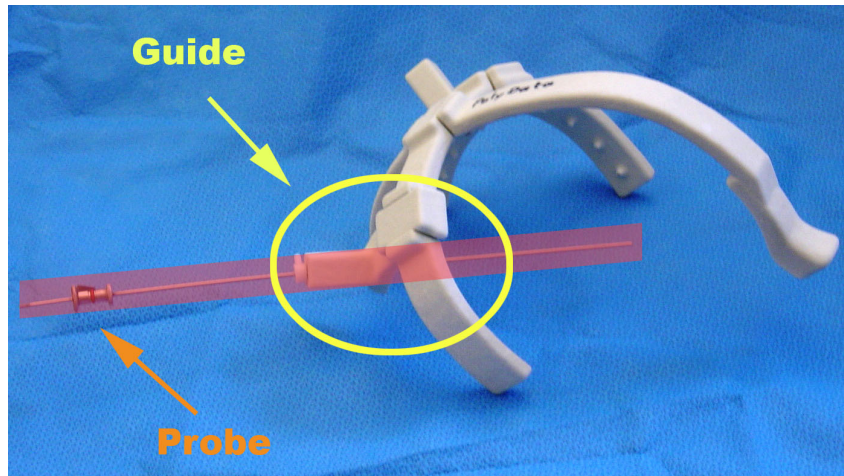


Figure 3.17: Fixture created using 3D printer with the guide to hold the probe.



Figure 3.18: Example of the fixture use.



Figure 3.19: Zprinter 310 three dimensional printer used to create the fixtures.

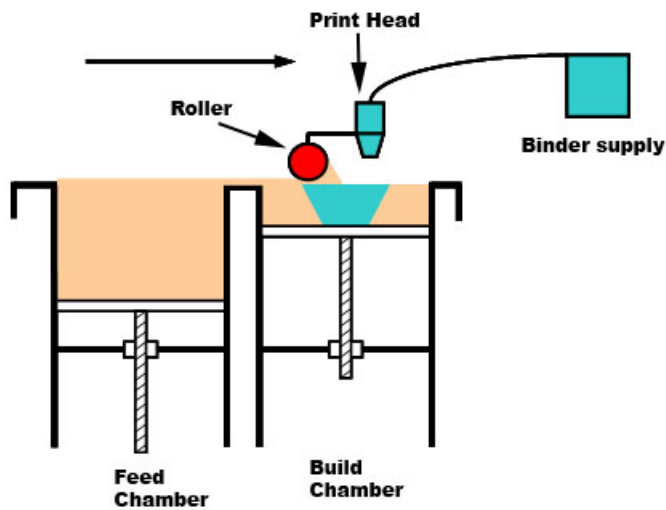


Figure 3.20: Zprinter 310 printing process.

### 3.3 Image domain segmentation techniques used in medical MRIs.

Different types of image segmentation techniques are applied in medical applications: region growing, clustering and active contours are commonly found.

### 3.3.1 Region growing

This algorithm starts with one or various seeds. From these a region grows by appending to each seed those neighboring pixels that have similar properties [9]. The main problem is to define the initial position of each seed. Usually in medical images such as MRI, the actual interest area is located near the center of the canvas; therefore the areas near the corners and sides can be considered the background and easily discriminated. This type of method is usually used to find tissue, for example the ventricles inside the brain can be segmented easily using image growing. There are problems when the region of interest is not completely enclosed which leads to undesired growth patterns.

### 3.3.2 Watershed

This technique starts with a topographical image in which region dissimilarities are encoded in higher altitudes [1]. Based on this map there are two algorithms that can be used for the segmentation. The first one floods the basins (minima) so the water level increases. When water from different valleys joins it is considered an edge.

The other method is called rain-falling, and the regions are segmented according to the path a water drop follows to reach a minimum or basin. Both of these methods are displayed in Figure 3.21.

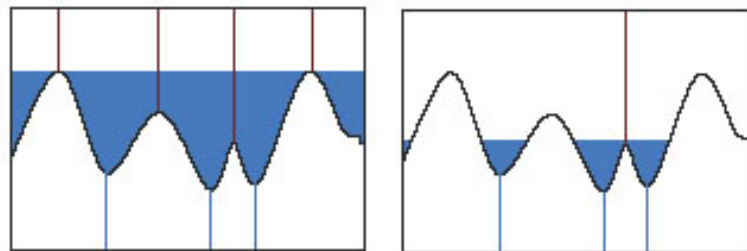


Figure 3.21: Watershed algorithms based on immersion (left) and rain-fall (right).

The disadvantage of using watersheds is the over segmentation, therefore other methods must be used in order to merge the regions. It is easier to identify regions by first using over-segmentation and then merging than having to detect the edges directly.

### 3.3.3 Active contours

Active contours are curves defined within an image domain that can move under the influence of internal forces within the curve itself and external forces derived from the image data [19].

Active contours "snakes" were proposed by [10]. This algorithm starts with a curve that is placed on the image and transforms its shape adapting to the contours of the specified region (Figure 3.22). In order to use this algorithm a model of the contour must be created (image attractor). This can be done using user pre-segmented images or by using a low-level algorithm that would define areas in which the object is contained.

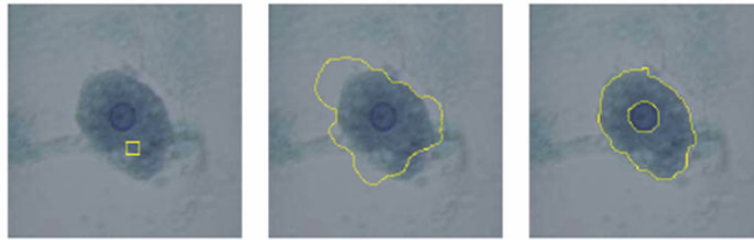


Figure 3.22: Example of how the snake adapts to the specific regions.

### 3.3.4 Active Shape Models

This technique was selected for the segmentation of the MR images and will be discussed in chapter 5.

## 3.4 Electronic and physical principles related to the solution

The advanced mathematical tools used in electronic engineering are directly applied into image processing. In order to fully understand the ASM concepts such as the principal component analysis, eigen decomposition and the Mahalanobis distance must be defined.

The segmentation process also conveys a great deal of knowledge within efficient programming and algorithm design.

# Chapter 4

## RESEARCH METHODOLOGY

### 4.1 Problem recognition and definition

The general problem was determined based on interviews with the head of the Radio surgery and radio Biology Laboratory Dr. Bova, and with assistant Scientist Dr. Rajon, main programmer for the rapid prototyping project.

The specific problem due to the MRI technical aspects was defined based on research papers and analysis of patient images.

### 4.2 Information gathering and analysis

Image segmentation techniques were reviewed from literature available at the laboratory and the university libraries. Current papers from different universities and institutes where also a large part of the research along with interviews with Dr. Rajon and other researchers from the department of electrical engineering.

### 4.3 Evaluation of the solution

In order to evaluate the algorithm an empirical discrepancy technique must be applied [22] for which the resulting image from the segmentation algorithm will be compared with "ground truth". The images included in the golden data will be obtained from the CT scans that have been registered against the MRI. The CT images show a large gray level difference between air and the patients skin surface. These values in accordance to the CT number correspond to 0 for air, 1000 for skin and 1800 for bone

approximately (CT numbers range from 0-4095). Because of these large differences a simple segmentation algorithm based on thresholding can be applied in order to determine the contour. The system implemented for the evaluation is shown in Figure 4.1.

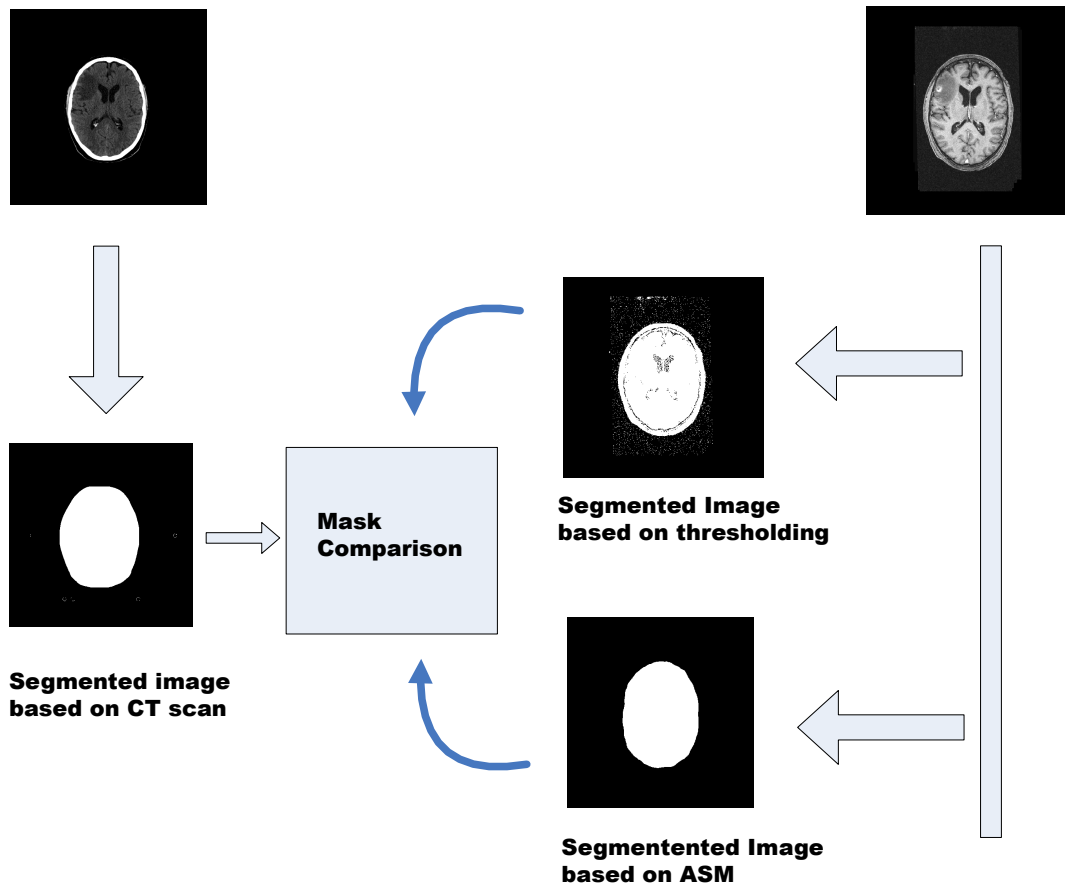


Figure 4.1: Scheme for the evaluation of the segmentation algorithms

## 4.4 Implementation of the solution

In order to develop the solution several stages were completed. First of all a bibliographical research on the most common segmentation methods in medical MRI was reviewed. Based on these papers and interviews at the department an adequate algorithm based on active shape models was designed.

Data pre- and post- processing modules were also implemented in order to make the results compatible with the software developed at the institute.

## 4.5 Evaluation and re-design

At the end of this thesis several recommendations have been made for a more robust and accurate technique using the ASM.

Image processing techniques are constantly improving as well as the hardware used in their implementation.

This constant growth in new algorithms will surely allow various improvements to the final solution in the near future.



# Chapter 5

## SOLUTION

### 5.1 Solution selection

A number of features can be used for image segmentation, these can be determined from image based information or from real world knowledge.

Segmentation is better understood in context with image recognition under the human visual perception. Marr-Palmer's computational vision framework in Figure 5.1 describes the process of object recognition. Image-based processing detects simple features like edges or corners. These salient features are then used by the surface-based processing block to create surfaces. Surfaces are assigned to objects in the object-based stage. The role and relationship with other objects in the scene is determined in the last category-based processing block [1]. Feedback in the blocks reflect a bilateral and iterative process in human object recognition.

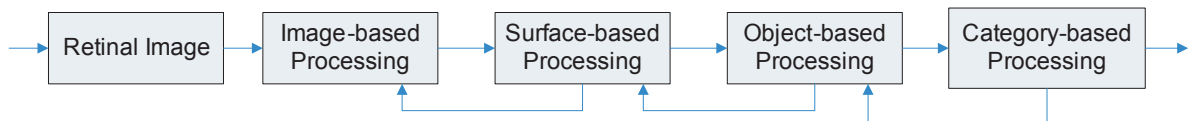


Figure 5.1: Marr-Palmer's computational vision framework for human perception.

Based on the first three stages of Marr-Palmer's model, segmentation techniques may be grouped as follows:

- Image-based segmentation: uses only the information contained in the camera image to find regions defined by low-level homogeneity criteria.
- Surface-based segmentation tries to find regions that correspond to real-world surfaces.

- Object-based segmentation detects real-world objects, by grouping regions of the surface-based segmentation using high-level knowledge.

As stated above image segmentation does not only depend on information given at the pixel level but also depends on a-priori knowledge. For example when creating surfaces it is expected that the edges be continuous lines, therefore if the segmentation at lower levels suggest divided edges these can be assumed as continuous in the surface detection block.

Each one of these categories can be subdivided [1]. Other categorizations do exist as the one used by [18]:

- Thresholding
  - Threshold detection methods.
  - Optimal thresholding.
  - Multi-spectral thresholding.
  - Thresholding in hierarchical data structures.
- Edge-based segmentation
  - Edge image thresholding.
  - Edge relaxation.
  - Border tracing.
  - Border detection as graph searching.
  - Border detection as dynamic programming.
  - Hough transform.
  - Region construction from borders.
- Region-based segmentation
  - Region merging.
  - Region splitting.
  - Splitting and merging.
  - Watershed segmentation.

Because of the vast number of techniques and their possible combinations, different solutions can address the same problem. In order to select the most appropriate method a detailed description of the information provided from the images and the context is required.

Figure 5.2 shows a typical MRI scan. The first aspect that needs to be considered is the MRI scanner itself. The gray values in images depend directly from the scanner that is being used as can be seen in Figure 5.3.



Figure 5.2: Example of an MRI scan.

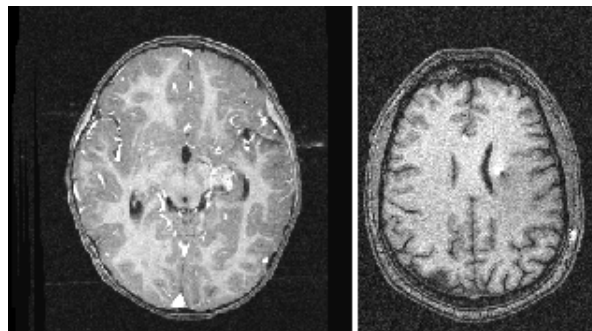


Figure 5.3: Examples of two MR images taken from different scanners.

Because the images can be generated from arbitrary machines it is important to have a pre-processing block that will filter out most of the variations. For this project histogram equalization and a median filter were applied. A median filter has the property of preserving the location of the edges, which is not true for others such as the Gaussian filters. After filtering is completed the magnitude of the gradient is calculated in order to decrease small variations along the gray values and increase the salient features in the image.

Another problem presented in the scanner is the partial volume effect. This phenomena occurs when the signals generated by the relaxation of the hydrogen protons are redirected and combined into the same voxel. Therefore the result is an averaged

image of the object scanned. It is easier seen during the process of a CT scan shown in Figure 5.4. During the scan radiation originated from the source doesn't travel in a straight line and therefore hits the object at a certain angle, depending on the composition of the objects these rays may be re-oriented and combined. This will create an image that represents an average of the original. Basically each pixel in the final image can represent more than one structure. This effect can be decreased by using a higher resolution. The partial volume effect is more complex and only a general idea has been presented here.

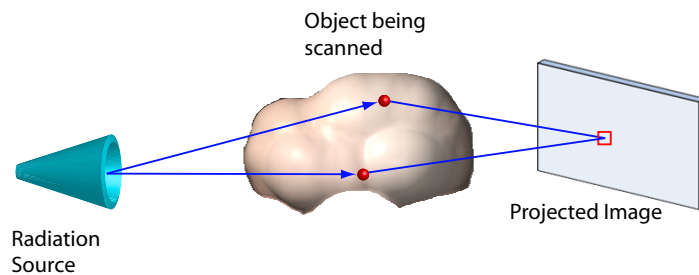


Figure 5.4: Partial volume effect.

MRI scanners in the process of creating an image use the inverse Fourier transform. This will cause repetitions of the original scan to appear. Figure 5.5 shows a scan at the top of the head in which the smaller oval represents the top portion and the larger shape around it is actually the bottom part of the head near the lips reappearing on the higher slices.

This last image shows another problem in MR imaging. There is a considerable signal loss as the scans near the top of the head in some cases the skin border may appear discontinuous because of this attenuation.

Because of all the variables and different scenarios present in a MRI scan, prior information becomes an important factor to consider when designing the segmentation algorithm. Image based techniques only refer to pixel level information, therefore if the borders are not continuous or there is great attenuation these methods are prone to fail. Region-based methods such as split/merge, region growing and watersheds, are usefull as approximations to the border, but because no prior information is included the final result may contain odd head shapes, discontinuous edges or even false borders.

The current method being used to generate the 3-D models is based on thresholding, and most of the problems can be seen on the top of the head because of the signal loss. Advanced methods such as level set or active contours [10] also known as "snakes" assume that the borders are continuous, which is a favorable aspect. But these methods will also fail because they do not make use of prior information.

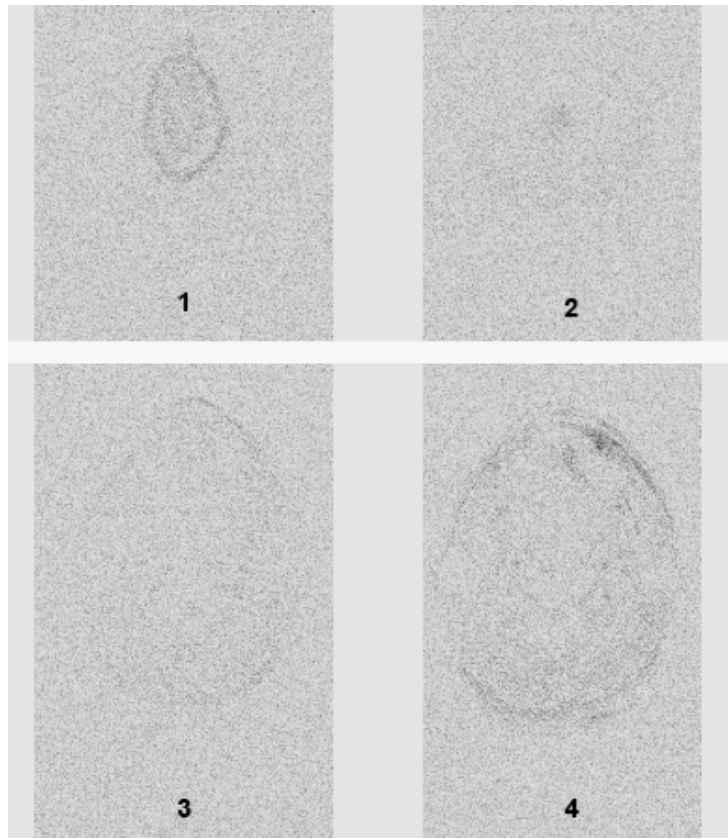


Figure 5.5: The inverse Fourier transform will cause bottom slices to reappear on the top slices.

Active contours are based on an energy minimization problem. A balance between the internal energy of the spline and the external energy obtained by the image is searched for. The internal energy refers to the elasticity and rigidity of the spline. The external energy involves the actual image information specially the salient features. The reason this method is likely to fail is that convergence on false edges is possible and there is no restriction on the shapes that may form when using these methods. For example, at slices near the eye level convergence on the brain cortex is highly probable.

Various combinations of the methods mentioned above are possible, for example watersheds or region growing techniques can be used to determine and approximate location of the head skin contour this approximation can be used to initialize an active contour in order to compensate for the discontinuous borders. But once again there are no constraints on the shapes generated.

When considering these aspects active shape models (ASM) [3] present the best characteristics. Similar to the active contours they are referred to as smart snakes [4]. ASM represent shapes as a set of points that may vary according to plausible defor-

mations considered during the training stage. This method of segmentation includes real world knowledge by using examples of head contours.

Image segmentation is only part of the project. Figure 5.6 shows a block diagram of the implemented solution divided into 4 modules:

- Pre-processing of the 3-D dataset.
- Offline creation of the shape and profile models.
- The active shape model module.
- Reconstruction of the 3-D dataset.

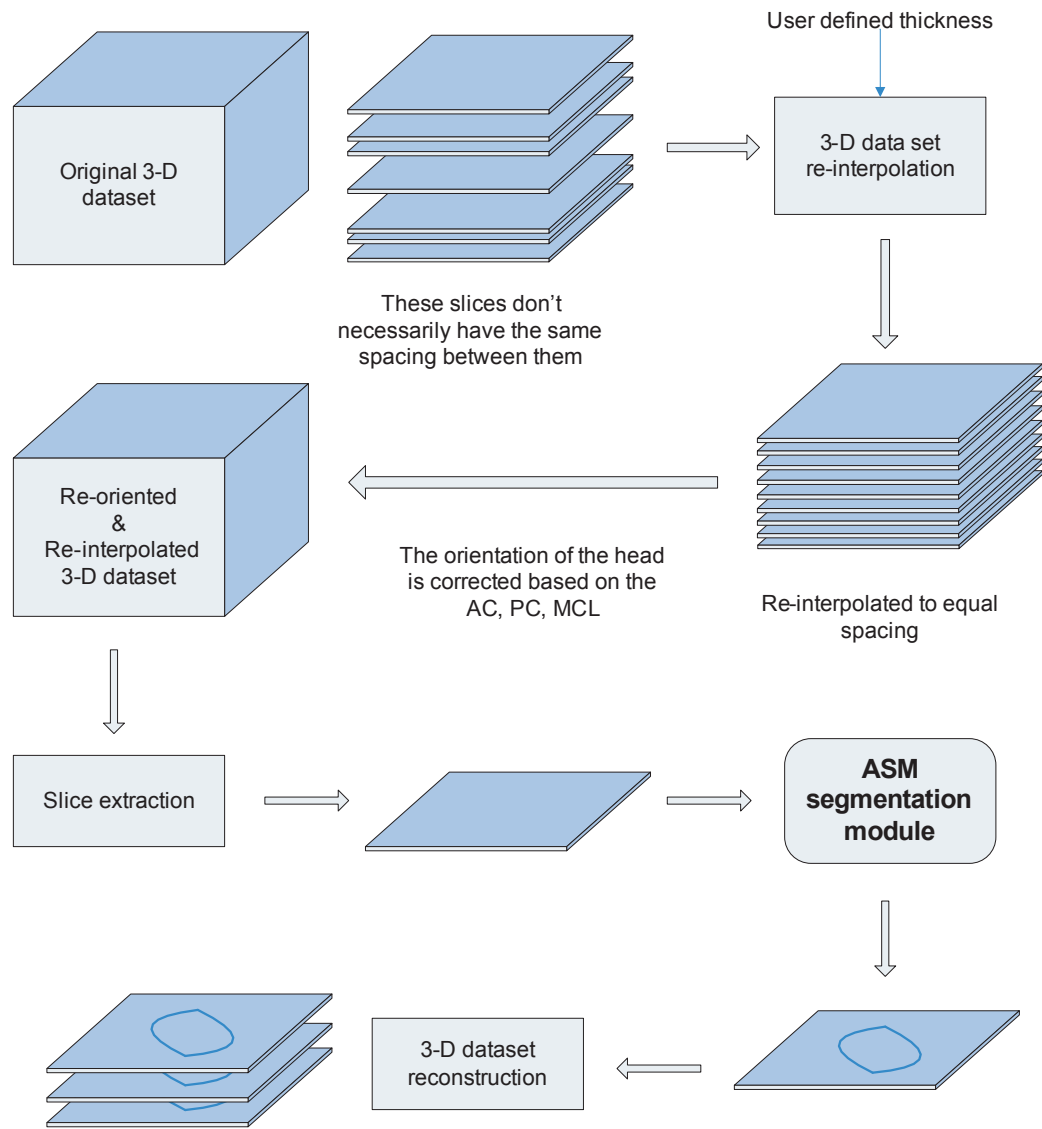


Figure 5.6: Block diagram for the general solution.

## 5.2 Active shape models

A shape model can be expressed in general as:

$$X = f(b) \quad (5.1)$$

Changing the values of  $b$  will generate new values for  $X$  which are determined by the model  $f$ , therefore  $b$  can be considered a descriptor of  $X$ . In the case of shape models the variation of the  $b$  parameters will generate new shapes and if the values of  $b$  are constrained, only certain shapes may be expressed.

Shape is considered as the quality of a configuration of points which is invariant under some transformation. The similarity transformations (translation, rotation and scaling) are considered for 2-D and 3-D shapes.

Shapes can be expressed as a set of  $n$  paired coordinates  $(x, y)$ :

$$\mathbf{x} = (x_1, y_1), (x_2, y_2), (x_3, y_3) \cdots \quad (5.2)$$

Rearranging the elements in equation 5.2 allows shapes to be expressed as a  $2n$  dimensional vector:

$$\mathbf{X} = \begin{bmatrix} x_1 \\ \vdots \\ x_n \\ y_1 \\ \vdots \\ y_n \end{bmatrix} \quad (5.3)$$

ASM capture the shape variations of an object into a model by using principal component analysis (PCA). This is a method for identifying patterns in data and once they have been found this data can be compressed. The method for PCA is detailed here.

### 5.2.1 Principal Component Analysis (PCA)

In order to use the principal component decomposition there are several steps. In this case shapes are expressed using the  $2n$  dimensional vector format.

The first step in PCA is to subtract the mean value of the data. By doing so the new mean of the data is zero.

The second step consists in calculating the covariance matrix. The covariance between 2 variables expresses how these variables vary in relation to each other. The covariance matrix can be calculated from the expression:

$$\mathbf{S} = \frac{1}{s-1} \sum_{i=1}^n (x_i - \bar{x})(x_i - \bar{x})^T \quad (5.4)$$

where  $s$ , is the number of shapes described using the  $2n$  dimension vectors.

The third step is to calculate the eigenvectors and eigenvalues of the covariance matrix. The normalized eigenvectors represent the direction in which the data varies in relation to the mean. The eigenvalues refer to how much of the data varies in the direction of the corresponding eigenvector. Figure 5.7 shows a cloud of 3D data points.

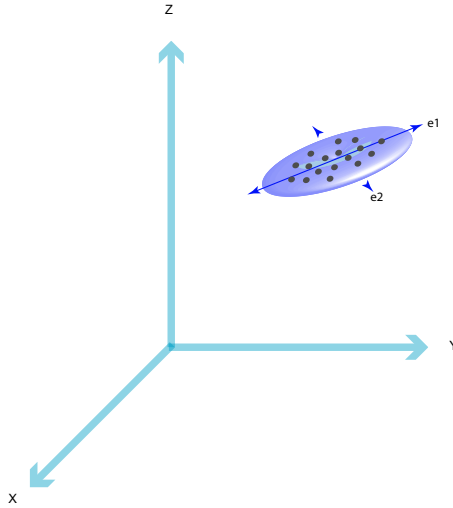


Figure 5.7: Illustration of the eigenvectors for a set of 3D points.

Because there are 3 dimensions the covariance matrix  $\mathbf{S}$  is:

$$\mathbf{S} = \begin{bmatrix} S_{x,x} & S_{x,y} & S_{x,z} \\ S_{y,x} & S_{y,y} & S_{y,z} \\ S_{z,x} & S_{z,y} & S_{z,z} \end{bmatrix} \quad (5.5)$$

where  $S_{x,y} = S_{y,x}$ ,  $S_{x,z} = S_{z,x}$ ,  $S_{z,y} = S_{y,z}$ , therefore this matrix is symmetric and each element in the diagonal expresses the variance of each dimension in the vector. The total variance is represented by the sum of all the elements in the diagonal. Certain properties apply in the eigen decomposition of the covariance matrix, first the sum of the eigenvalues  $\lambda$  is equal to the sum of the values in the diagonal which corresponds

to the variance in each dimension. Therefore  $\sqrt{\lambda} = S.D.$ , where S.D. is the standard deviation for that dimension.

The number of eigenvectors will be the same as dimensions in the matrix. For the distribution 3D points in Figure 5.7 the eigenmatrix is:

$$\begin{bmatrix} \phi_1^1 & \phi_2^1 & \phi_3^1 \\ \phi_1^2 & \phi_2^2 & \phi_3^2 \\ \phi_1^3 & \phi_2^3 & \phi_3^3 \end{bmatrix} \quad (5.6)$$

For which the eigenvectors are organized as columns vectors:

$$e_1 = \begin{bmatrix} \phi_1^1 \\ \phi_2^1 \\ \phi_3^1 \end{bmatrix} \quad e_2 = \begin{bmatrix} \phi_1^2 \\ \phi_2^2 \\ \phi_3^2 \end{bmatrix} \quad e_3 = \begin{bmatrix} \phi_1^3 \\ \phi_2^3 \\ \phi_3^3 \end{bmatrix} \quad (5.7)$$

Each one of these vectors has an associated eigenvalue  $\lambda^1, \lambda^2, \lambda^3$ . The original dataset may be expressed as a combination of the mean value and a weighted sum of the eigenvectors:

$$\mathbf{X} = \bar{x} + \Phi \mathbf{B} \quad (5.8)$$

In this case the column vector  $B$  represents the weights for the dimensions in the eigenvectors.

$$\mathbf{B} = \begin{bmatrix} b_1 \\ b_2 \\ \vdots \\ b_t \end{bmatrix} \quad (5.9)$$

If we consider the data in Figure 5.7, the variation occurs mainly along two dimensions therefore one of the eigenvectors can be ignored, this eigenvector will correspond to that which has the lowest eigenvalue and thus expresses the least variance. This determines the fourth step which is to consider only the eigenvectors that represent most of the variance in the dataset. This will allow for data compression by multiplying each value in the dataset by the truncated eigenmatrix.

This multiplication transforms the data into a subspace known as eigenspace. The data can also be transformed back by using the inverse of the eigenmatrix, which is the same as the transpose of the matrix, because the eigenvectors are orthonormal among themselves.

PCA is fundamental in understanding the development of ASM. In this case the vectors will not be 2 or 3 dimensional, they will have twice as many dimensions as points used to describe the shapes.

## 5.2.2 Shape modelling

The main idea behind the ASM is being able to represent shape variation in a compact model.

First the mean shape is determined, along with the covariance matrix and its eigen decomposition. This allows shapes to be expressed using the model:

$$x \approx \bar{x} + \Phi \mathbf{B} \quad (5.10)$$

where,  $\Phi = (e_1 | \dots | e_t)$

The number of eigenvectors or modes considered in the model can be chosen based on the percent of variance expressed. In the implementation of the ASM the eigenvectors were arranged in descending order considering the respective eigenvalues. The number of modes used for the model were those that when added expressed 96% of the total variance.

The model is created by using a set of training shapes that will define the matrix  $\Phi$ . If the number of training shapes used is less than the dimensions of the shape then the number of eigenvectors will be equal to the number of training shapes [3].

This model can also be used to generate new shapes by varying the parameters in the  $\mathbf{B}$  column vector. The elements in this vector will weigh a dimension in each eigenvector as seen in equation 5.11:

$$x = \bar{x} + \Phi \mathbf{B}$$

$$\begin{bmatrix} x_1 \\ \vdots \\ x_{2n} \end{bmatrix} = \begin{bmatrix} \bar{x}_1 \\ \vdots \\ \bar{x}_{2n} \end{bmatrix} + \begin{bmatrix} \phi_1^1 & \cdots & \phi_1^t \\ \vdots & \vdots & \vdots \\ \phi_{2n}^1 & \cdots & \phi_{2n}^t \end{bmatrix} \cdot \begin{bmatrix} b_1 \\ \vdots \\ b_t \end{bmatrix} \quad (5.11)$$

The first dimension of the shape  $x_1$  can be expressed as the mean plus a weighted sum of the first element in every eigenvector:

$$x_1 = \bar{x}_1 + \phi_1^1 \cdot b_1 + \cdots + \phi_1^t \cdot b_t \quad (5.12)$$

Therefore each shape can be characterized by its corresponding  $\mathbf{B}$  vector. In order to determine a plausible shape the distribution of the  $b$  elements must be calculated. In this case it will be assumed that the elements in the  $\mathbf{B}$  vector are independent and Gaussian. This means that all plausible shapes will be defined by  $\mathbf{B}$  vectors for which all elements have been constrained to:

$$\begin{aligned} -3 \cdot S.D. < b_i < +3 \cdot S.D. \\ -3 \cdot \sqrt{\lambda_i} < b_i < +3\sqrt{\lambda_i} \end{aligned} \tag{5.13}$$

The assumption that the elements in the  $\mathbf{B}$  vectors are Gaussian is valid to represent the shapes of head contours because the variation is continuous. If the training set were instead shapes that showed only two distant possible variations then the probability density function for the  $b$  elements would show 2 spikes for which any of the values in between would generate invalid shapes.

By varying the elements of the  $\mathbf{B}$  vector under the constraints, new shapes can be created. Figure 5.8 shows how the variation of each of the dimensions affects the mean shape, for a case in which the shapes are hands.

These shapes are defined by a group of points which are selected based on specific landmarks. The location of these landmarks is a complex problem specially if done automatically.

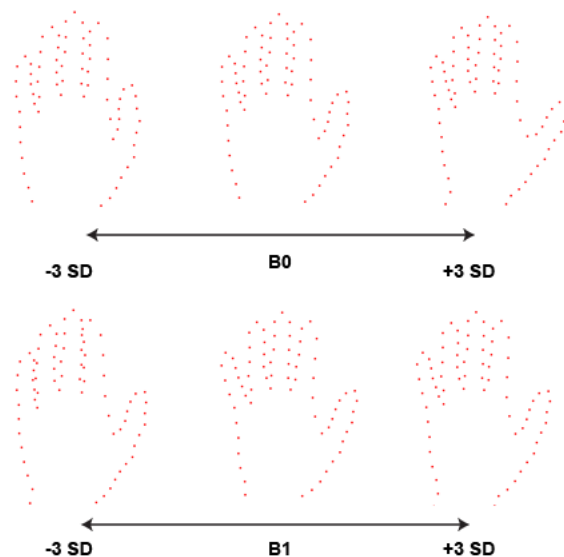


Figure 5.8: Effect of varying the elements in the  $\mathbf{B}$  vector. The shapes have been scaled and translated in order to be displayed.

### 5.2.3 Landmarks

Landmarks are points that can be specifically located from one training image to another [3] (Figure 5.9), which means there is a correspondence between the points. The labeling of the training shapes can become a tedious task if done manually for 2D or 3D datasets. Some authors have used a minimum description length approach to select the landmarks automatically with promising results [16].

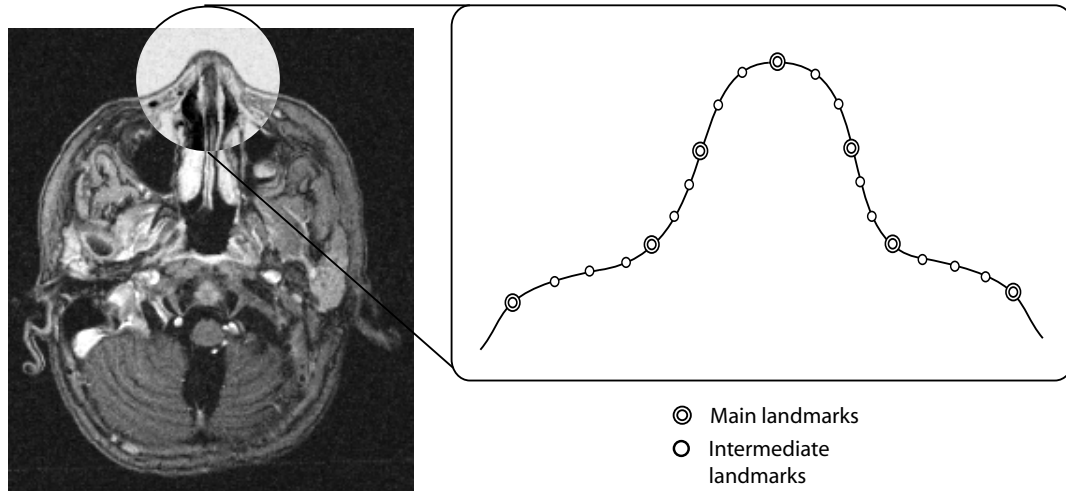


Figure 5.9: Landmark assignment near the tip of the nose.

For this project manual point correspondence was used. The simplicity of the human head contour allowed for an easy identification of important anatomical landmarks such as the tip of the nose and the eyes. Other methods used for automatic landmark placement in medical imaging combine the use of registered CT and MR images.

Skin surfaces can be easily identified in CT scans, but they will not match the MRI scan entirely because during the CT scan the patient is wearing a head ring, while during an MR scan the patients head is pushed against the table. The different scenarios for the scans will produce inconsistencies in the contour of the rear part of the head.

### 5.2.4 Training set

The training images must be selected carefully because they will determine the plausible shapes allowed by the model.

The most influential factor in the shape from one person to another is the age. The available patients from which the training set was created had a Gaussian distribution

as seen in Figure 5.10. Because each patient has his or her own unique characteristics the shapes have arbitrary scaling, translations and rotations that must be normalized through out the set.

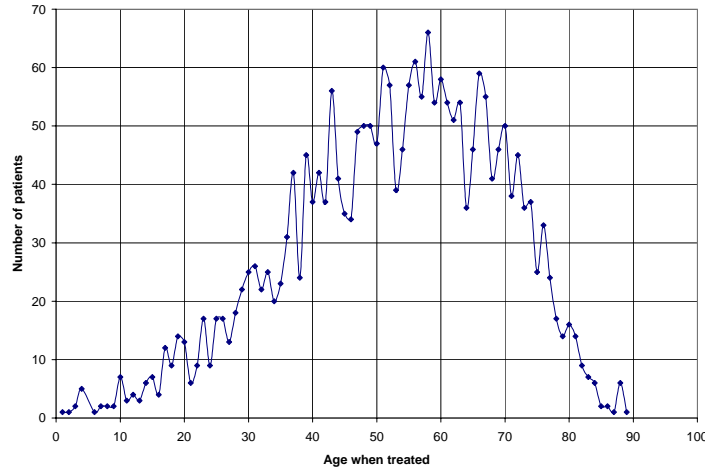


Figure 5.10: Distribution of the patients by age at treatment in the radiosurgery database at the McKnight Brain Institute.

In order to align the training set the following method has been implemented [3]:

1. Translate each example so that its center of gravity is at the origin.
2. Choose one example as an initial estimate of the mean shape and scale so that  $|\bar{x}| = 1$
3. Record the first estimate as  $\bar{x}_0$  to define the default reference frame.
4. Align all the shapes with the current estimate of the mean shape.
5. Re-estimate the mean from the aligned shapes.
6. Apply constraints on the current estimate of the mean by aligning it with  $\bar{x}_0$  and scaling so that  $|\bar{x}| = 1$
7. If not converge, return to 4.

This method will converge when the value of the mean does not change significantly.

In order to align two shapes,  $x_1$  to  $x_2$ , first,  $x_1$  and  $x_2$  are translated to the origin where the average angle and distance between every set of corresponding points is calculated, then shape  $x_1$  is re-oriented and scaled using these values, finally  $x_1$  is translated so the center of gravity of  $x_1$  matches the original center of gravity of  $x_2$ . Other methods for shape alignment can be used to minimize distances between both shapes [7].

It is important to recall that this model expresses only shape variation. The algorithm that morphs the shape is discussed in the following section.

## 5.2.5 Model morphing

For the shape model to become active another stage is required. This stage is known as model morphing. It uses image-based information obtained from the training images (not specifically the shapes) to determine the best movements of each point in the shape. Figure 5.11 shows the main idea. In order to determine the new suggested shape the Mahalanobis distance is used.

In order to calculate the Mahalanobis distance a model for the magnitude of the gradient for the gray level values along the normal profile that intersects each point in the shape is determined. The profile for each point is calculated based on the adjacent points as shown in Figure 5.12.

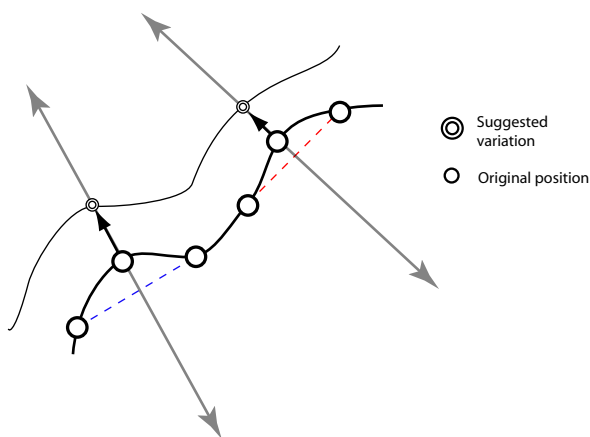


Figure 5.11: Point based displacements.

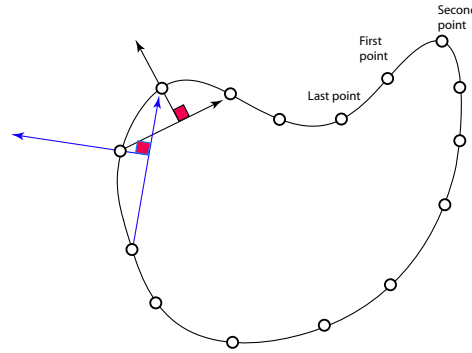


Figure 5.12: Gray level profile creation based on adjacent points.

Therefore a vector  $g$  of size  $k$  will be assigned to each point and it will contain the magnitude of the gradient that has been divided by the sum of the elements to normalize (5.14):

$$\hat{g}_{i,j} = \frac{g_{i,j}}{\sum_l (|g_{i,j,l}|)} \quad (5.14)$$

where the index  $i$  corresponds to a specific point in the shape,  $j$  represents the training image on which the shape is located and  $l$  iterates through the elements in the specified  $g$  vector. With this in mind a  $g$  vector will be created for each point of the shape on each one of the shapes in the training set.

With this set of  $g$  vectors a profile model can be created for each one of the points in the shape. Similar to the shape model, a mean  $g$  vector  $\bar{g}_i$  and covariance matrix  $S_{g_i}$  is calculated for each point. These models are created based on a profile that contains  $k$  values of gray levels. Once the mean  $g$  vectors and covariance matrix have been calculated the Mahalanobis distance of any other  $g$  vector of size  $k$  can be calculated by using (5.15):

$$f(g_i) = (g_i - \bar{g}_i) \cdot S_g^{-1} \cdot (g_i - \bar{g}_i)^T \quad (5.15)$$

To determine the displacement for a specific point a larger profile is selected of size  $m$ . This larger profile is scanned using a  $k$  size profile that will be evaluated with the Mahalanobis distance. The vector that results in the smallest distance is considered to be the best fit and will determine the displacement for the point. This is illustrated in Figure 5.13.

Once all the points have been moved to their suggested displacements a new shape is formed. This shape doesn't necessarily represent a valid shape, therefore shape

constraints are applied. In order to apply these constraints the elements in the  $B$  vector are determined from the current shape based on equation 5.16:

$$\mathbf{B} = \Phi^T(x - \bar{x}) \quad (5.16)$$

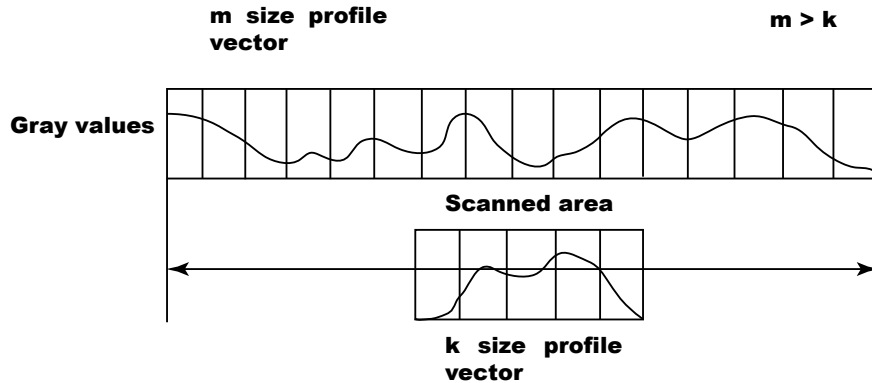


Figure 5.13: Profile scanning.

Because it was assumed that every element has an independent and Gaussian distribution, they have been limited to  $\pm 3S.D.$  therefore any element outside these limits will be forced to the maximum variation depending on their sign.

This is an iterative process between new shape suggestions given by the profile model and shape constraints determined by the shape model. At this point the algorithm is considered an active shape model. Figure 5.14 shows the suggested shape in red and the constrained shape in blue as it can be seen the ASM converges on the edges.

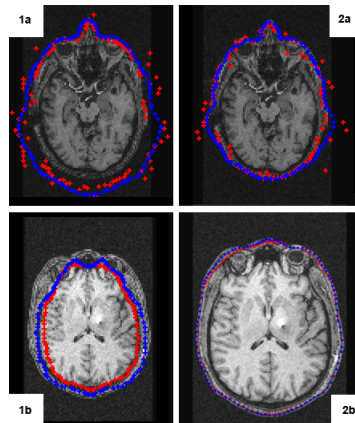


Figure 5.14: The suggested shape in red and the shape when the constraints are applied in blue. Figures 1a and 2a show this process at the nose level. Figures 1b and 2b are near the AC-PC plane.

## 5.2.6 Initialization

An important factor that has great influence in the speed of convergence of the model is the initialization of the model. Similarity transformations will be applied to the shape  $x$ , therefore the shape converging on the image will be:

$$X = T_{(s,\theta)} \cdot [x] + T_x \quad (5.17)$$

The initial values for the scaling, rotation and translation define the shape initialization.

Various methods may be used to determine the similarity transformation parameters, including region-based segmentation techniques and genetic algorithms, but in this case an easier approach was applied. Although initialization is an important decisive factor for the convergence of the ASM if a multi-resolution framework is used the importance of the initialization is decreased and the mean shape of all the training images can be used as a good starting point.

## 5.2.7 Multi-resolution framework

The multi-resolution framework consists in smoothing and subsampling the image at lower resolutions. This approach can be seen as a pyramid (Figure 5.15). First the shape is initialized at its mean value and placed on the lowest resolution, once the ASM has converged it is transferred to a higher resolution image this continues until the original resolution is reached. This method will increase the rate at which the ASM converges and will decrease the probability of an erroneous segmentation.

## 5.2.8 ASM features

Some of the advantages of using the ASM are [5]:

- The same algorithm is applicable to various problems by simply changing the training set.
- Expert knowledge can be captured and applied to the segmentation.
- The models give a compact representation of plausible shape variations, but are specific enough not to allow arbitrary variation different from that seen in the training set.

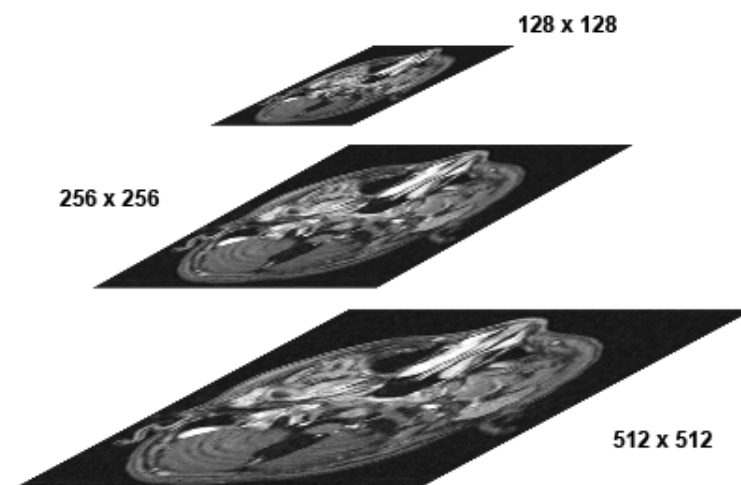


Figure 5.15: Multi-resolution framework.

The ASM have been able to detect objects in the presence of noise and warping of the shapes as seen in Figure 5.16.

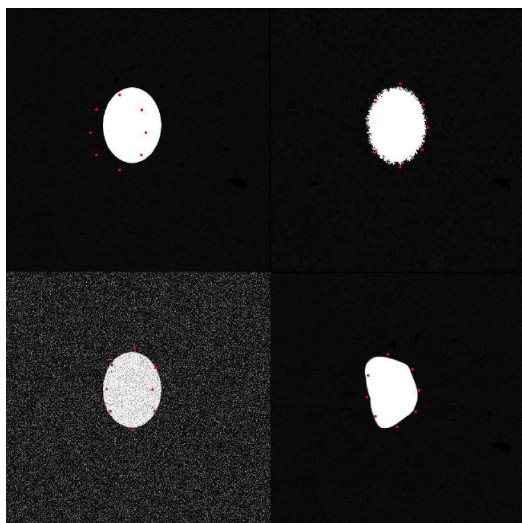


Figure 5.16: Intermediate tests applied to the ASM during the implementation. The test image was transformed by adding noise, warping and smoothing.

Before the 3D datasets could be segmented using the ASM a prior stage was required in order to prepare the data, as explained in the next section.

### 5.3 3D dataset pre-processing

When a patient is placed in the MRI scanner (Figure 5.17), his body is moved through the magnetic field by sliding the table on which he is laying down. The slices obtained by the scan don't necessarily have the same separation in the direction of the moving table (axial coordinate). The information given by the scanner contains an axial coordinate measured in millimeters which refers to the patients position on the table.



Figure 5.17: Setup in the MR scanning room.[8]

In order to create a uniformly spaced dataset the original set is linearly interpolated. The thickness of these slices may be adjusted by the user. The interpolation of the slices is required for the next step.

Another variant in MRI scanning is the position of the patients head. Figure 5.18 shows a sagittal cut in which the head is tilted. If these variations are large non linear transformations in the shape of the skin border will occur when the data set is sliced along the axial coordinate. These shapes cannot be expressed by the active shape model and therefore the segmentation will be flawed.

In order to correct for the miss alignment three anatomical landmarks are identified.

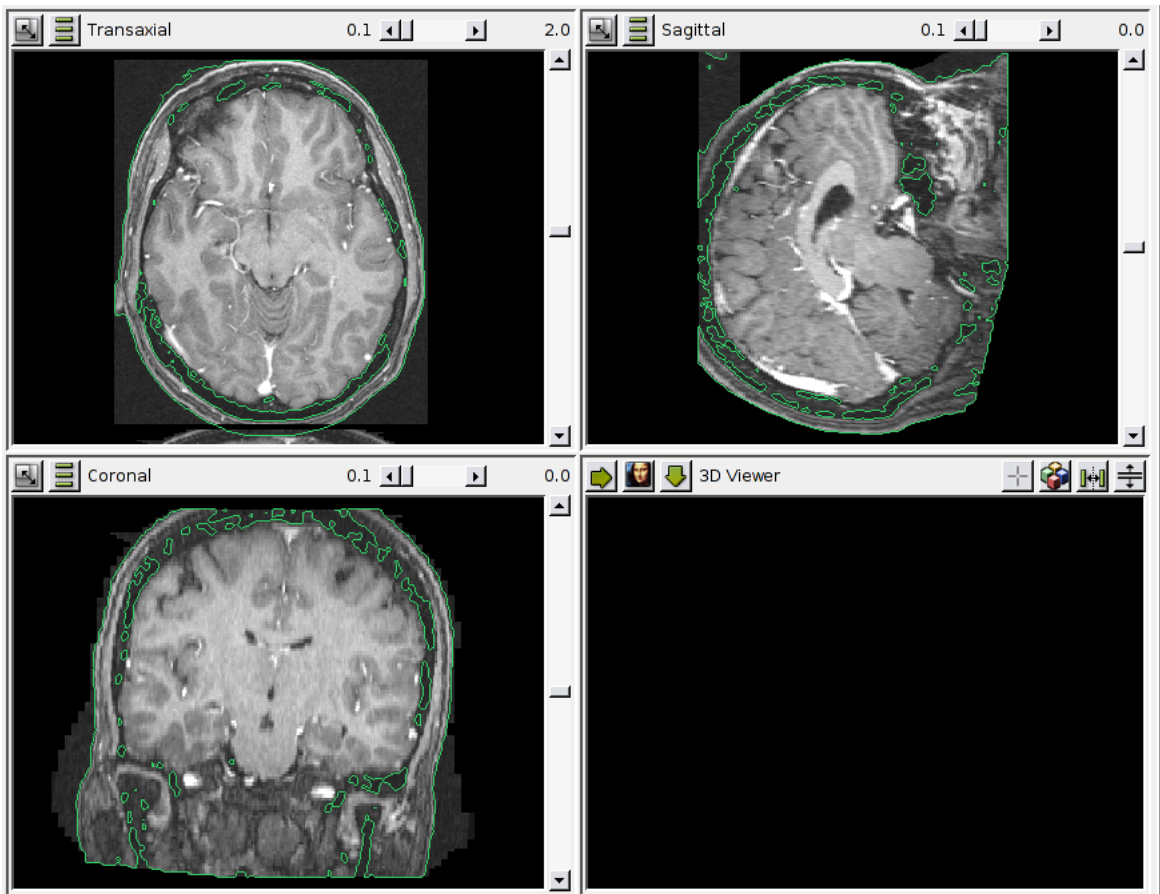


Figure 5.18: The patients head can be tilted as seen in the sagittal view (lower left).

### 5.3.1 Data set re-orientation

Before calculating the transformation matrix a coordinate system must be defined. The MRI scans provide information about the axial coordinate and the axial slice spacing in millimeters. The axial coordinate may have arbitrary values depending on the scanner and the position of the patient. The number of slices may also vary.

The 3-D dataset will be interpreted in a world coordinate system. For which the line  $(0, 0, z)$ , will cross every slice at the center and the position of each slice along the  $z$  axis will be given by its axial coordinate as seen in Figure 5.19, the dataset is spread in the direction of the  $x$  and  $y$  axis based on the spacing determined by the scanner. This spacing is constant for all axial slices.

Based on this reference 3 anatomical landmarks will be selected in order to apply the transformation matrix. The location of these landmarks requires a specialist.

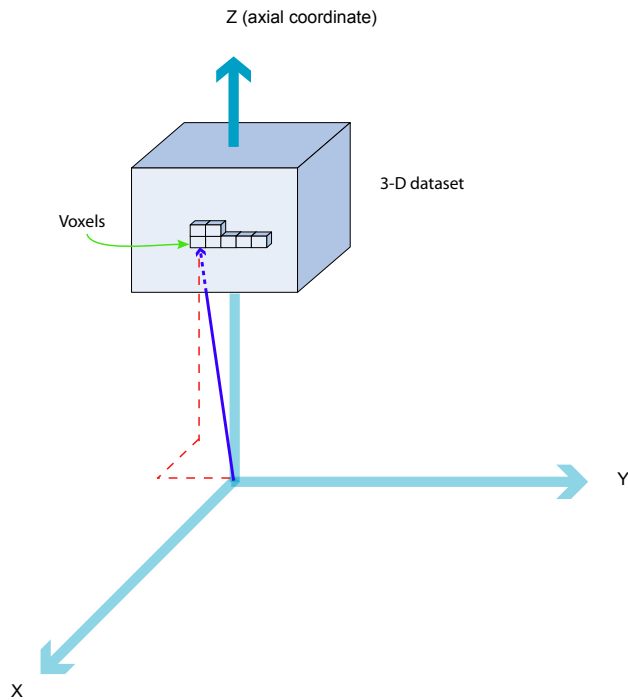


Figure 5.19: 3-D dataset interpreted in a world coordinate system.

### Anatomical landmarks for image re-orientation

These landmarks correspond to the Anterior Commissure (AC), Posterior Commissure(PC) and mid sagittal line or mid center line(MCL). The typical location for these points can be seen in Figure 5.20.

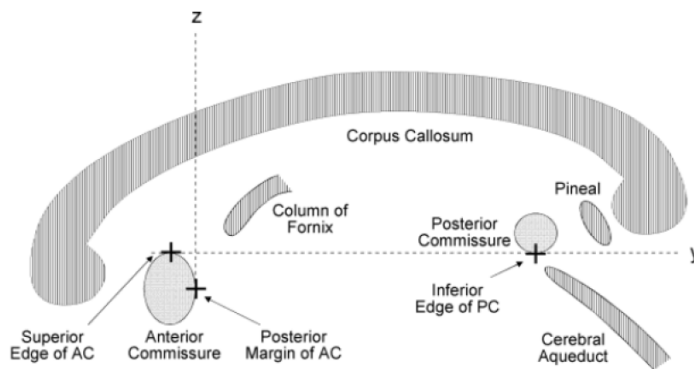


Figure 5.20: Location of the anatomical landmarks. [6]

The implementation of an automatic identification algorithm for these landmarks is also a complex problem. Figure 5.21 shows the landmarks selected manually, the problem becomes complex when even a specialist must undergo an iterative process to determine these points.

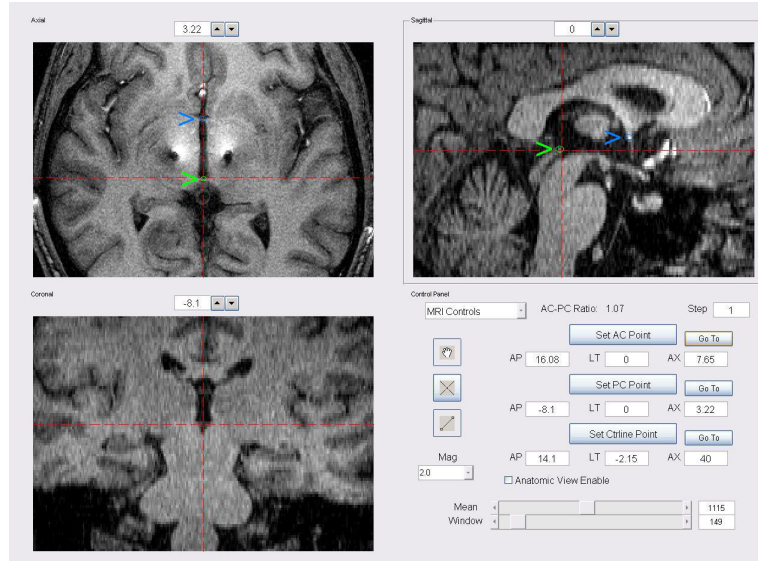


Figure 5.21: Identification of the landmarks.

The middle point between the AC and PC will be considered as the center of the head and the origin of the anatomical coordinate system. The transformation required to re-orient the data set will take place over this point.

The vector from PC to AC will determine the direction of the positive  $y$  axis, the  $z$  axis is calculated based on the MCL and the vector determined by the cross product of  $y$  and  $z$  will define the  $x$  axis. Figure 5.22 shows the coordinate system based on the anatomical landmarks.

Equations (5.18) are used to determine the normalized vectors that describe the orientation of the head.

$$\begin{aligned}
 \hat{x} &= \frac{\hat{y} \times \hat{z}}{\|\hat{y} \times \hat{z}\|} \\
 \hat{y} &= \frac{AC - PC}{\|AC - PC\|} \\
 \hat{z} &= \frac{(MCL - PC) - \hat{y}[(MCL - PC) \cdot \hat{y}]}{\|(MCL - PC) - \hat{y}[(MCL - PC) \cdot \hat{y}]\|}
 \end{aligned} \tag{5.18}$$

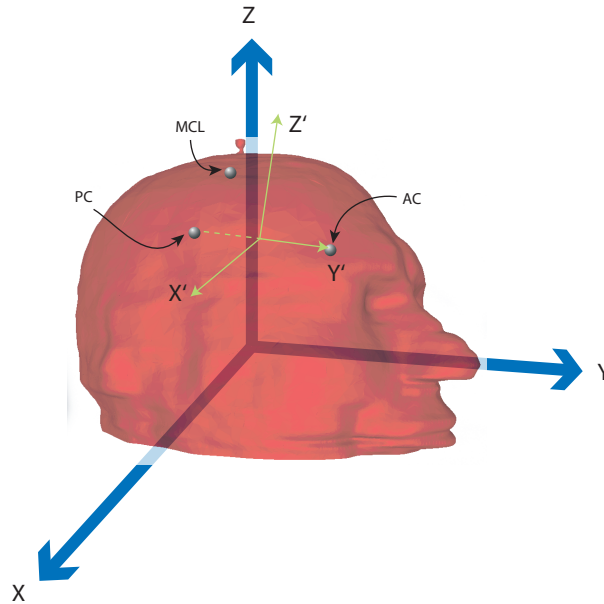


Figure 5.22: Coordinate system defined by the anatomical landmarks.

With these equations the relative angles between both coordinate systems are known and can be used to determine the transformation matrix. To do so three methods that can be applied:

- Direction Cosines.
- Euler angles.
- Euler Parameters.

The use of the direction cosines is considered to be a brute-force approach and is not applicable to video rendering or 3D graphics. Figure 5.23 shows coordinate systems F1 and F2, where F2 is the result of transforming F1 using the direction cosines matrix.

The transformation matrix using the direction cosines in 5.19 has 9 variables, although it can be proven that only three of them are necessary. This approach was used in the implementation because the calculation of the transformation matrix was only done once. This is not the case of a moving object in which coordinate system transformations are required at every displacement, in these cases quaternions are usually applied.

$$\begin{bmatrix} V_{x_2} \\ V_{y_2} \\ V_{z_2} \end{bmatrix} = \begin{bmatrix} \cos(\theta_{x_2,x_1}) & \cos(\theta_{x_2,y_1}) & \cos(\theta_{x_2,z_1}) \\ \cos(\theta_{y_2,x_1}) & \cos(\theta_{y_2,y_1}) & \cos(\theta_{y_2,z_1}) \\ \cos(\theta_{z_2,x_1}) & \cos(\theta_{z_2,y_1}) & \cos(\theta_{z_2,z_1}) \end{bmatrix} \begin{bmatrix} V_{x_1} \\ V_{y_1} \\ V_{z_1} \end{bmatrix} \quad (5.19)$$

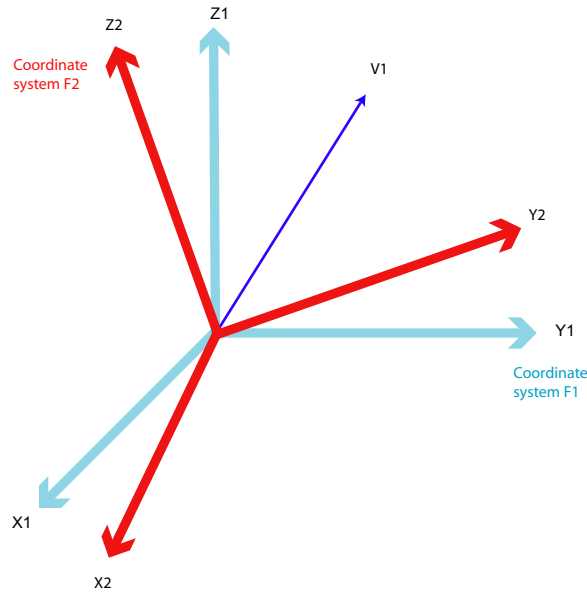


Figure 5.23: Coordinate transformation.

In order to determine the direction cosines matrix the angle between the axis of both coordinate systems must be known, these can be calculated using the normalized vectors obtained from the AC, PC and MCL.

To reduce the number of computations when the dataset is transformed the inverse transformation is used. Each pixel position in the re-oriented system F2 will be transformed back to F1 and interpolated using trilinear interpolation 5.20.

$$\begin{aligned}
 \text{InterpolatedValue} = & B_0 \cdot (1 - x) \cdot (1 - y) \cdot (1 - z) \\
 & + B_1 \cdot x \cdot (1 - y) \cdot (1 - z) \\
 & + B_2 \cdot x \cdot y \cdot (1 - z) \\
 & + B_3 \cdot (1 - x) \cdot y \cdot (1 - z) \\
 & + B_4 \cdot (1 - x) \cdot (1 - y) \cdot z \\
 & + B_5 \cdot x \cdot (1 - y) \cdot z \\
 & + B_6 \cdot x \cdot y \cdot z \\
 & + B_7 \cdot (1 - x) \cdot y \cdot z
 \end{aligned} \tag{5.20}$$

The variables  $B_0, B_1, B_2, B_3, B_4, B_5, B_6$  and  $B_7$ , correspond to 8 known values that surround the point that will be interpolated as can be seen in Figure 5.24.

Based on the inverse transformation matrix obtained from the direction cosines and the trilinear interpolation the patients head can be re-oriented and normalized.

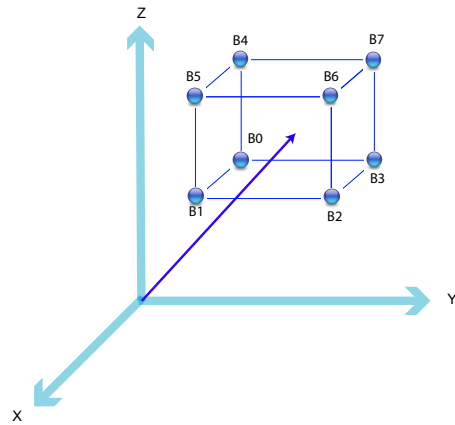


Figure 5.24: Basics of trilinear-Interpolation.

## 5.4 3D Dataset reconstruction

After the segmentation of a slice has been performed using the ASM, the final result can either be a border around the skin contour leaving the rest of the image intact or the result can be a binary mask. Either way these segmented slices are then grouped into a 3-D dataset which can be used to create a surface of the patients head in order to continue with the general process for the rapid prototyping.

# Chapter 6

## RESULTS AND DISCUSSION

### 6.1 ASM overview

Figure 6.1 shows the initialization of the ASM. The average similarity transformations in the training set were used for the initialization. There were 113 points used to describe the contour of the head. The first tests were done with only 56 points. The results obtained were poor, the nose curvature wasn't described correctly and therefore appeared as jagged lines in the final segmented image.

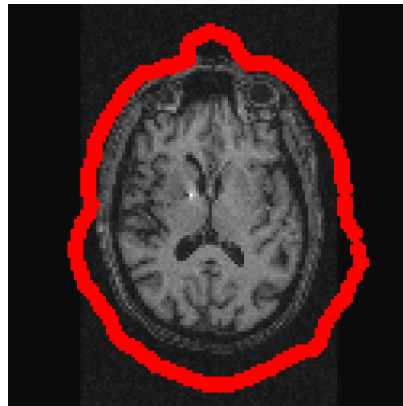


Figure 6.1: Active shape model initialization.

In order to obtain better results the head was divided into 2 regions based on the AC-PC plane. One model was created for the top of the head and another for the bottom which includes mostly the nose and the lips of the patient depending on the amount of information available from the scan.

From each one of these models two others were created to comply with the multi-resolution framework. In total six models were implemented:

- Above the AC-PC plane.
  - Original 512 x 512 resolution
  - 256 x 256 resolution
  - 128 x 128 resolution
- Under the AC-PC plane.
  - Original 512 x 512 resolution
  - 256 x 256 resolution
  - 128 x 128 resolution

Each one of these models includes both the shape model and the profile model. One of the main advantages of ASM is the fact that the number of training images can be nearly unlimited because the creation of the model is done offline. The end result is simply the mean shape, the eigen decomposition, a mean profile vector and an inverted covariance matrix list for the profile model.

Figures 6.2, 6.3 and 6.4 show the process of convergence of the ASM at different resolutions. The iterations start with an image that has been downsampled and filtered using a Gaussian mask to a resolution of 128x128 pixels. In this case convergence occurred in 10 iterations. Convergence can be defined when the distance between the expected shape and the original shape reaches a threshold.

Once the ASM has converged the resolution is increased until the original resolution is achieved.

One of the advantages of using these 3-D datasets is that the variation between two consecutive slices is minimum. This was exploited during the implementation by using the multi-resolution framework only on the slice defined by the AC-PC plane. The next slices used the previous position and only the 512x512 model was applied.

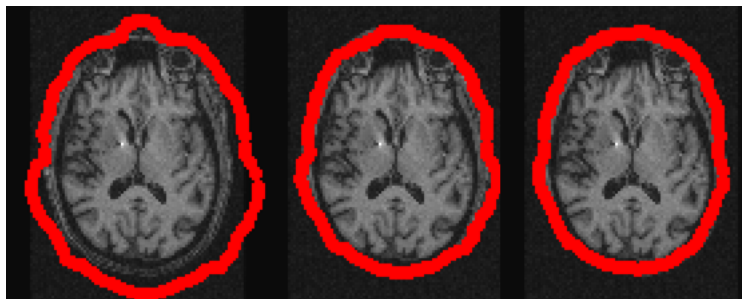


Figure 6.2: Active shape model converging at a resolution of 128x128.

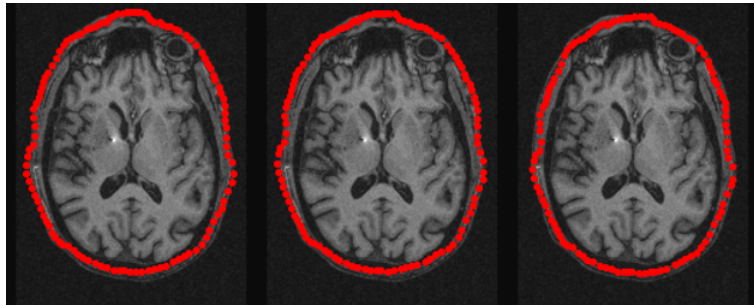


Figure 6.3: Active shape model converging at a resolution of 256x256.

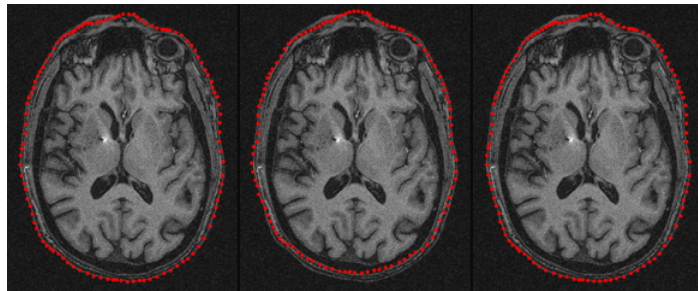


Figure 6.4: Active shape model converging at a resolution of 512x512.

## 6.2 Results at specific depths in the brain

The following sections show the final position of the ASM at different depths in the head.

### 6.2.1 Over the AC-PC plane: Top of the head

One of the major problems of using thresholding is the effect of signal loss in slices near the top of the head. Figure 6.5 shows convergence of the ASM even though the borders are faded and discontinuous. This can also be appreciated in the 3-D models shown in Figure 6.11.

Because the objective is the detection of the skin surface the shape of the ears have been simplified in order to represent the shapes using the model. The problem with the ears is their complex shape that varies radically from one patient to another. These variations are due to natural causes and the conditions in which the person is scanned. In some cases the ears are pushed against the head causing unpredictable deformations.

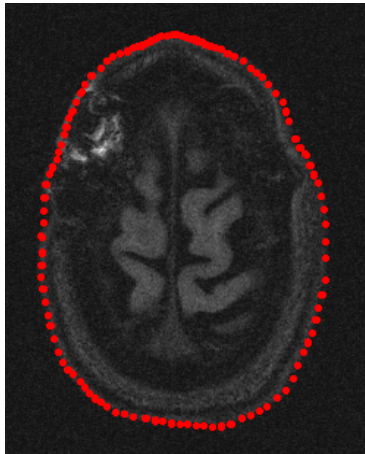


Figure 6.5: ASM converging on a slice near the top of the head.

### 6.2.2 Under the AC-PC plane: nose curvature

After the top part of the head has been segmented the model is switched (nose model). The main characteristic of these slices is the shape of the nose. Figure 6.6 shows the convergence of the ASM on one of these slices. In this case the nose has been well detected, but because of the anatomy of the nose false border detection becomes an eminent problem as will be shown in the next section.

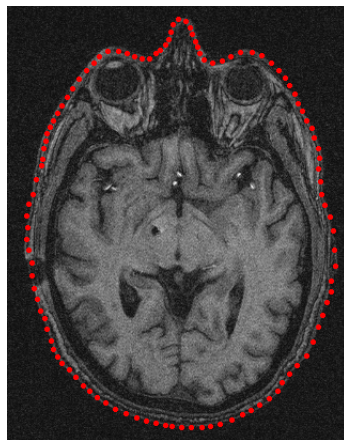


Figure 6.6: ASM converging on a slice under the AC-PC plane.

## 6.3 Comparison obtained using thresholding and ASM

Although the previous results give a good idea of how well the ASM works a more quantitative approach is needed. Direct comparisons between the results obtained

using thresholding methods and ASM will be considered in the following.

In order to compare both methods, registered CT and MRI scans were used. But the entire contour was not accounted for, only the patients face was used to compare the results because the rear of the head usually does not match between the CT and MRI. This occurs because during the MR scan the patient is laying down on his back with his head against the table, while during the CT scan the patients head is surrounded by the stereotactic headring.

The figures shown in this section correspond to the mask obtained from both segmentation techniques over-imposed on the mask generated by the CT, which is used as the reference point for comparisons.

### 6.3.1 Over the AC-PC plane: Top of the head

As a final result of the segmentation process the program is able to deliver either a binary mask of the skin contour or a boundary conserving the rest of the original data. For the comparisons a binary mask was created for both the thresholding and ASM.

Figure 6.7 shows the superposition of the ASM and thresholding results over to copies of the CT reference. Both segmentation techniques seem to return similar results. The problem with thresholding is more clearly viewed in the 3-D images in the following section.

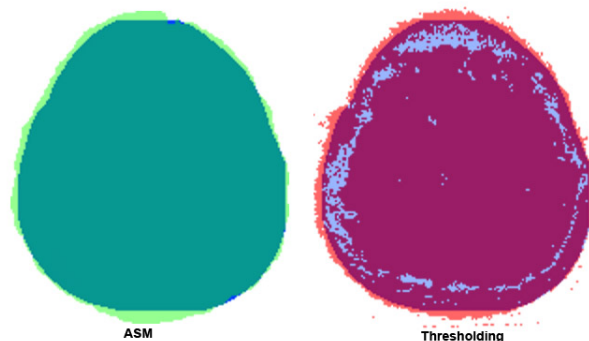


Figure 6.7: Superposition of the mask generated by the ASM and thresholding over the CT reference for a slice near the top of the head. Blue: CT reference. Red: mask generated by thresholding. Green: mask generated by the ASM.

### 6.3.2 Near AC-PC plane

Most of the slices between the top and the AC-PC plane show little variation in their shape. There is also little signal attenuation. As expected both methods produced similar results (Figure 6.8).

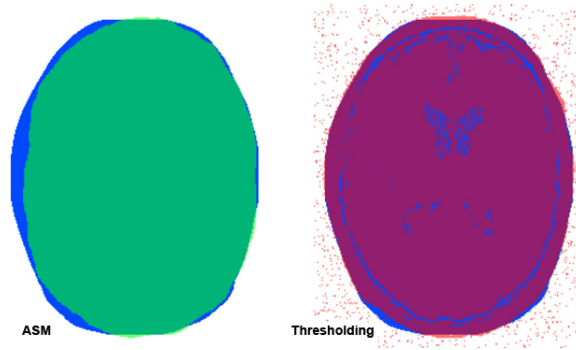


Figure 6.8: Superposition of the mask generated by the ASM and thresholding over the CT reference for a slice above the AC-PC plane. Blue: CT reference. Red: mask generated by thresholding. Green: mask generated by the ASM.

### 6.3.3 Under the AC-PC plane: nose curvature

For slices under the AC-PC plane the figure of the nose begins to appear. In Figure 6.9 the ASM performed as expected because the shape variation was clearly expressed in the training set and the borders are visible.

One of the main difficulties for the ASM at these levels is the large shape variations that occur near the tip of the nose which are hard to contemplate in the training set. This is specially true when the nostrails are exposed. These rapid changes cause the convergence on false borders.

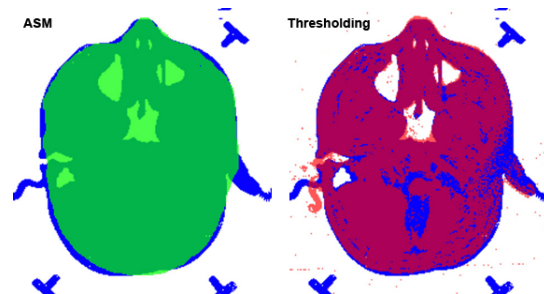


Figure 6.9: Superposition of the mask generated by the ASM and thresholding over the CT reference for a slice at the nose level. Blue: CT reference. Red: mask generated by thresholding. Green: mask generated by the ASM.

Finally in order to measure how well each algorithm detects the skin border referring to the segmented CT image as the "ground truth" the following technique was applied (see Figure 6.10).

1. The CT image was segmented using thresholding which led to a binary image.
2. Landmarks were located along the image contour.
3. Because both CT and MRI have been fused they will overlap. The points from the CT are transferred on top of the mask generated by the ASM.
4. The square of the distances between each point to the nearest border is calculated.
5. The sum of these distances is considered the segmentation error.
6. The same procedure is applied for the MR image segmented using thresholding

These measurements were applied to the results shown in Figures 6.7, 6.8, 6.9 and table 6.1 was generated.

These results show that both methods produce similar results for slices above the AC-PC plane, but differ for the nose slices. In order to improve these results a number of parameters can still be varied within the algorithm along with various pre-processing techniques. Some of the parameters set for the ASM are the profile size used to create the model, the size of the profile scanned, and the amount of variance that will be allowed by the shape model. Other improvements include combinations with region based segmentation techniques and thresholding.

Table 6.1: Sum of the square of the border differences between the segmentation results and the reference CT scan (15 points were used).

	<b>ASM</b>	<b>Threshold</b>
Head top	145	122
Middle	362	136
Nose	468	212

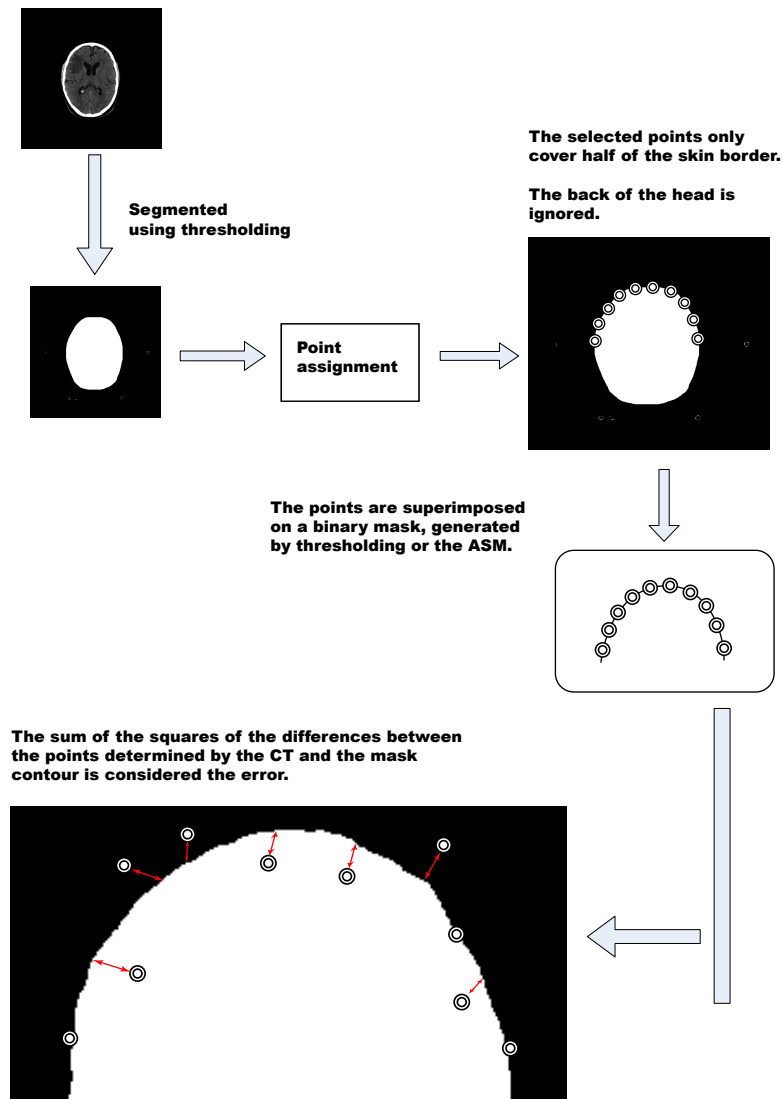


Figure 6.10: Procedure to determine how well the segmentation algorithms perform.

## 6.4 3D model generation

3D models generated from the slice based segmentation are used as a qualitative measurement of both segmentation algorithms.

Figure 6.11, shows the result obtained using thresholding. It can be seen that near the top of the head the signal loss causes part of the brain cortex to be visible.

One of the advantages of thresholding is that complex features such as the ears and the nostrils can be easily determined from these images. The main difference is at

the top of the head for which the ASM produced closed contours around the head while the thresholding produced disconnected contours which lead to exposure of the brain cortex.

Problems with the ASM are clearly visible at nose level slices (Figure 6.12). The shape of the nose presents rough steps near the bottom which are a consequence of false edge detection as will be shown in the next section.

Finally Figure 6.13 shows the superposition of both results, in which the difference stated before are clearly visible.

The principal and most useful advantage of the ASM is border completion at higher levels which show promising results for future work.

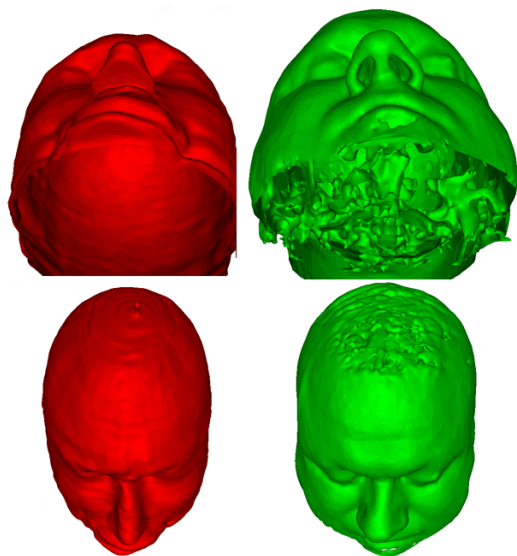


Figure 6.11: Qualitative comparison between the ASM results (left) and thresholding (right).



Figure 6.12: Surface generated by the ASM.



Figure 6.13: Qualitative comparison between the ASM results and thresholding applying superposition.

## 6.5 Processing Time

The processing time for a  $512 \times 512$  slice is approximately 0.8 seconds on a laptop with an Intel M 1.4 Ghz processor and 512MB of RAM. To complete an entire 3-D data-set it takes about 2 minutes depending on the number of slices which usually ranges around 100.

## 6.6 Future work

Some of the problems that still need to be addressed are discussed here.

### 6.6.1 False edge detection

At depths near the bottom of the nose and the lips false edge detection becomes a problem as shown in Figure 6.14. For which the ASM has converged erroneously. In order to compensate for these errors a larger training set can be used. Other options include dividing the head in more sectors than just the 2 mentioned before. Combination with the thresholding results could also help constrain shape deformations and avoid these problems.

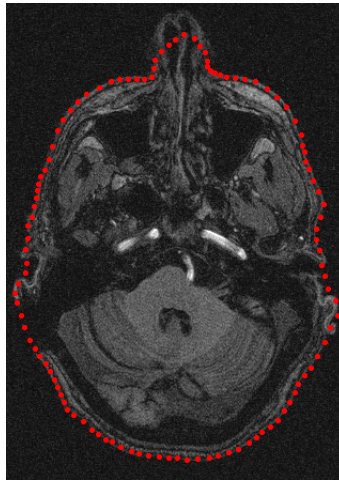


Figure 6.14: ASM converging on a false edge.

### 6.6.2 Pre-processing

A robust pre-processing module is required in which the variations of the intensity from different machines can be normalized

Another consideration is the fact that the DICOM datasets have been cropped and reformatted into what is known as "mimg" and "ximg". These two formats correspond to fused MR and CT images which have been cropped automatically to decrease the file size.

Because of this cropping every slice in the dataset could have a different size but are all padded to fit a  $512 \times 512$  matrix. Intermediate filters can be added before the padding in order to improve the salient features of the images. Different padding techniques could also be tested.

### 6.6.3 Shape variation in young patients

An important consideration is that the patients selected for the training set had been treated during their 30s and 40s. Pediatric patients show different shapes for their head contour. Organ distribution inside the head also doesn't match the one of an adult therefore if more models are used to express different sectors of the head the parameters assigned for the selection of the model have to be carefully adjusted. A solution to this problem would be to normalize the size of the head based on the distance between the AC and PC.

#### **6.6.4 Automatic landmark placement**

One of the options for automatic landmark placement, is the use of an expert fused CT and MR pair. The only considerations that must be accounted for are the variations in the rear part of the head and the point to point correspondence which could become a complex problem.

# Chapter 7

## CONCLUSIONS AND RECOMMENDATIONS

### 7.1 Conclusions

- The time required for the segmentation of a 512x512 image using the ASM is 0.7s.
- The implementation is compatible with the current rapid prototyping system.
- The discrepancy evaluation method used is only valid for contours on the face of the patient. The rear of the head cannot be compared using a CT as the ground truth for MRI segmentation.
- To remove non-linear transformations in the dataset when analyzed as axial slices 3D re-orientation is required.
- ASM are useful for general shape variations, but when the variations are local, convergence on false borders is possible.
- The models used by the ASM can be determined offline and therefore do not add to the actual processing duration.
- The number of landmarks used to describe the shape was 113. These were enough to describe features like the nose. Using 56 points lead to jagged borders when the masks were created.
- Results depend not only on the number of images used in the training set but also the variability expressed in these images.
- Multi resolution framework increased the possibility of correct convergence.

- Discontinuous and diffused borders were correctly detected using the ASM.
- ASM generated promising results for head contour detection at slice above the AC-PC plane. But would converge on false borders for slices near the nose level.
- The surface generated by the segmentation using ASM is still not applicable to the rapid prototyping project.

## 7.2 Recommendations

- Constrain the suggested movements to avoid overlapping between the points.
- Test other pre-processing algorithms.
- Use area-based techniques such as region growing and watersheds to aid the ASM.
- Implement an automatic landmark assignment algorithm based on the fused pairs of CT and MR images.
- Increase the variability of the training set including patients from all ages.

# Bibliography

- [1] Pablo Alvarado. *Segmentation of color images for interactive 3D object retrieval*. RWTH Aachen, 2004.
- [2] Jerrold T. Bushberg, J. Anthony Seibert, Edwin M. Leidholdt Jr, and John M. Boone. *The Essential Physics of Medical Imaging*. Lippincott Williams and Wilkins, Philadelphia, 2001.
- [3] T. F. Cootes, C. J. Taylor, D. H. Cooper, and J. Graham. Active shape models - their training and application. *Comput. Vis. Image Underst.*, 61(1):38–59, 1995.
- [4] T.F. Cootes, A. Hill, C.J. Taylor, and J. Haslam. Active shape models - 'smart snakes'. In *British Machine Vision Conference (BMVC)*, pages 266–275. Springer-Verlag, 1992.
- [5] T.F. Cootes and C.J. Taylor. *Statistical Models of Appearance for computer vision*. Manchester, UK, 2004.
- [6] Robert W. Cox. Afni: Software for analysis and visualization of functional magnetic resonance neuroimages. *Comput. Biomed.*, 29:162–173, 1996.
- [7] T. F. Cootes et al. Training methods of shape from sets of examples. In *British Machine Vision Conference (BMVC)*, pages 9–18, Leeds, UK, 1992.
- [8] Utah Center for Advanced Imaging Research. [cited 18 January 2006]. Available from the World Wide Web: <http://www.ucair.med.utah.edu/Graphics/3T-MRI-scanner-cropped-med.png>.
- [9] Rafael C. Gonzalez and Richard E. Woods. *Digital Image Processing*. Addison-Wesley Longman Publishing Co., Inc., Boston, MA, USA, 2001.
- [10] M. Kass, A.P. Witkin, and D. Terzopoulos. Snakes: Active contour models. *IJCV*, 1(4):321–331, January 1988.
- [11] Smith KR, Frank KJ, and Bucholz RD. The neurostation-ahighly accurate, minimally invasive solution to frameless stereotactic neurosurgery. *Comput Med Imaging Graph*, 18(4):247–256, 1994.

- [12] Alan Wee-Chung Liew and Hong Yan. Current methods in the automatic tissue segmentation of 3d magnetic resonance brain images. *Current medical imaging reviews*, 2(1), 2006.
- [13] Department of neurosurgery McKnight Brain Institute.
- [14] Neurosurgery Focus 2003 American Association of Neurological Surgeons, 2003. [cited 1 September 2005]. Available from the World Wide Web: <http://www.medscape.com/content/2003/00/44/83/448307/art-nf448307.fig4.gif>.
- [15] Nikhil R. Pal and Sankar K. Pal. A review on image segmentation techniques. *Pattern Recognition*, 26(9):1277–1294, 1993.
- [16] Tim F. Cootes Jhon C. Waterton Rhodri H. Davies, Carole J. Twining and Chris J. Taylor. A minimum description length approach to statistical shape modeling. *IEEE Transactions on medical imaging*, 21(5):525–537, 2002.
- [17] Siemens. Siemens. [cited 16 October 2005]. Available from the World Wide Web: <http://www.medical.siemens.com>.
- [18] Milan Sonka, Vaclav Hlavac, and Roger Boyle. *Image Processing: Analysis and Machine Vision*. O'Reilly, 1999. SON m 99:1 1.Ex.
- [19] Chenyang Xu and Jerry L. Prince. Gradient vector flow: A new external force for snakes. In *CVPR '97: Proceedings of the 1997 Conference on Computer Vision and Pattern Recognition (CVPR '97)*, page 66, Washington, DC, USA, 1997. IEEE Computer Society.
- [20] X. Yu, T. D. Bui, and A. Krzyzak. Robust estimation for range image segmentation and reconstruction. *IEEE Trans. Pattern Anal. Mach. Intell.*, 16(5):530–538, 1994.
- [21] Y. J. Zhang. A survey on evaluation methods for image segmentation. *Pattern Recognition*, 29(8):1335–1346, 1996.
- [22] Yu Jin Zhang. A review of recent evaluation methods for image segmentation. *International Symposium on signal Processing and its Applications (ISSPA)*, pages 530–538, 2001.

# Appendix A

## Glossary

**AC:** Anterior Commissure.

**ASM:** Active Shape Model

**ITK:** Insight ToolKit.

**MCL:** Mid Center Line.

**MRI:** Magnetic Resonance Image.

**PC:** Posterior Commissure.

**VTK:** Visualization ToolKit.



# Appendix B

## McKNight Brain Institute description

The McKnight Brain Institute at the University of Florida opened its doors the 22 of October, 1998. The purpose of the institute is to provide the intellectual and physical infrastructure to support rapid advances in the fundamental understanding of the normal and injured or diseased nervous system using the most contemporary tools in the research armamentarium and (b) support the development of multidisciplinary teams and approaches that are focused on rapidly translating these fundamental findings into clinical and commercial applications [9].

The different research areas involve :

- Age-related memory loss and cognition
- Brain cancer
- CNS injury, including post-traumatic and stroke
- Chronic neurological diseases (including movement disorders such as Parkinson's disease, multiple sclerosis, Alzheimer's disease, epilepsy, and neuromuscular disorders).
- Development, regeneration, and rehabilitation
- Mental health, neurobehavioral sciences, psychiatry (including schizophrenia, obsessive compulsive disorder, addiction)



# Appendix C

## Radiology and Radio Biology laboratory description

This laboratory contains a computer-controlled six Mev linear accelerator for use in cerebrovascular, cancer and fundamental cell and molecular research. To the best of our knowledge, this is still only full-time radiosurgery-biology research laboratory of its kind in the world [9].

A variety of studies take place in the lab including:

- Experiments to develop and evaluate techniques and equipment to be used in (CT, MRI and ultrasound) image-guided radiation therapy, intensity-modulated radiation therapy, image-guided radiosurgery, image-guided surgery and stereotactic surgery.
- Experiments to deliver single and multi-fraction radiation schedules to various radiobiological models (both cell and animal), including those designed to investigate the possible concomitant use of gene delivery and radiation therapy.
- Experiments to validate models used to predict dose distributions and dose models.